



## Article

# Combining Spatial–Temporal Remote Sensing and Human Footprint Indices to Identify Biodiversity Conservation Hotspots

Yuting Lu <sup>1</sup>, Hong Wang <sup>1,2,\*</sup>, Yao Zhang <sup>1</sup>, Jiahao Liu <sup>1</sup> , Tengfei Qu <sup>2</sup> , Xili Zhao <sup>1</sup>, Haozhe Tian <sup>1</sup>, Jingru Su <sup>1</sup>, Dingsheng Luo <sup>1</sup> and Yalei Yang <sup>2</sup>

<sup>1</sup> College of Geography and Remote Sensing Sciences, Xinjiang University, Urumqi 830046, China; 107552101101@stu.xju.edu.cn (Y.L.); zhangyao@stu.xju.edu.cn (Y.Z.); 107552103460@stu.xju.edu.cn (J.L.); 107552103482@stu.xju.edu.cn (X.Z.); 107552103458@stu.xju.edu.cn (H.T.); 107552203704@stu.xju.edu.cn (J.S.); 107552203697@stu.xju.edu.cn (D.L.)

<sup>2</sup> Faculty of Geographical Science, Beijing Normal University, Beijing 100875, China; qutengfei@mail.bnu.edu.cn (T.Q.); yangyalei@mail.bnu.edu.cn (Y.Y.)

\* Correspondence: wanghong@bnu.edu.cn

**Abstract:** Considering Inner Mongolia as the study area, the ecological theory of climate change, and human activities affecting a wide range of biodiversity patterns, MODIS multi-timeseries remote sensing image data were used and the interannual variation index was obtained by the method of fitting the curve to obtain the annual phenological and seasonal indicators. At the same time, the Landsat 8 standard deviation image was calculated to obtain the spatial variation index and generate spatial–temporal remote sensing indices to quantify the threat of climate change to biodiversity. In addition, the impact of human activities on biodiversity was quantified by generating a map of the human footprint in Inner Mongolia. The spatial–temporal remote sensing index and the human footprint index were integrated to identify areas protected from climate change and human activities, respectively. Eventually, the hotspot areas of biodiversity conservation in Inner Mongolia were obtained and priority protected area planning was based on the hotspot identification results. In this study, remote sensing technology was used to identify biodiversity conservation hotspots, which can overcome the limitations of insufficient species data from the past, improve the reliability of large-scale biodiversity conservation analyses, and be used for targeted management actions that have practical significance for biodiversity conservation planning.

**Keywords:** climatic change; human activities; biodiversity; hotspot identification



**Citation:** Lu, Y.; Wang, H.; Zhang, Y.; Liu, J.; Qu, T.; Zhao, X.; Tian, H.; Su, J.; Luo, D.; Yang, Y. Combining Spatial–Temporal Remote Sensing and Human Footprint Indices to Identify Biodiversity Conservation Hotspots. *Diversity* **2023**, *15*, 1064. <https://doi.org/10.3390/d15101064>

Academic Editor: Raúl Romero-Calcerrada

Received: 29 August 2023

Revised: 25 September 2023

Accepted: 26 September 2023

Published: 7 October 2023



**Copyright:** © 2023 by the authors. Licensee MDPI, Basel, Switzerland. This article is an open access article distributed under the terms and conditions of the Creative Commons Attribution (CC BY) license (<https://creativecommons.org/licenses/by/4.0/>).

## 1. Introduction

Biodiversity is declining at an unprecedented rate [1]. The establishment of protected areas is one of the key conservation strategies to prevent biodiversity loss [2], minimize habitat loss, and more effectively maintain threatened populations [3]. In response to the global decline of biodiversity, there has been a significant increase in the number of protected areas over the past two decades. Currently, there are more than 2 million areas of land that have been designated as protected areas, accounting for 15% of the global land area [4]. However, the existing coverage of protected areas is still insufficient to address the current biodiversity crisis. Therefore, it is necessary to increase the number of protected areas but, more importantly, establish the appropriate areas for protection [5]. Focusing on the priority protection of important areas is a more realistic and efficient way to protect biodiversity.

Large-scale patterns of biodiversity are strongly affected by climate change and human activity [6–10]. Rapid climate change poses a hazard to biodiversity by dramatically increasing the vulnerability of various species [11–13]. Additionally, phenology and temperature could also change seasonally due to climate change [14,15], which may result in

a phenological mismatch between species, the resources they rely on to reproduce, and their habitat characteristics [16]. Biodiversity is threatened when vegetation phenology and temperature vary greatly across years, outpacing the rate at which organisms can adapt [17–19]. In times of rapid climate change, enhancing adaptability during periods of high interannual fluctuation and high spatial variability in vegetation phenology and temperature can lessen the potential of biodiversity loss [20]. Since they offer a variety of resources, habitat conditions, microclimatic areas at small scales, and ecosystems with significant spatial variability [21], places with high spatial variability have better rates of species survival than areas with low spatial variability [22,23]. Similarly, the high spatial variability of surface temperatures provides microclimates that reduce the exposure of species to extreme temperatures and offer heat-protected shelters for species [24,25]. The satellite-based long timeseries vegetation index can effectively capture the seasonal interannual variation in the enhanced vegetation index (EVI) and land surface temperature (LST) to obtain phenological indicators [26–28]. The spatial variability feature can be captured by calculating the variability among pixels in a moving window, i.e., the image texture. Image textures are effective measures of habitat suitability for wildlife [29,30]. For instance, the 30 m resolution EVI's standard deviation picture texture features had a positive correlation with the overall number of native birds in the United States [29] and there was a good correlation between the abundance of native American birds and the standard deviation texture of the winter LST [31]. These examples illustrate that the standard deviation texture of images can be used to measure vegetation and temperature structures in relation to biodiversity.

Not only do spatial–temporal changes in climate affect biodiversity, but human activities have also dramatically altered the terrestrial biosphere, leading to land conversion, global biogeochemical changes, and loss of biodiversity [32,33]. Since the 20th century, the rapid growth of global population and the disturbance of global ecosystems by human activities has increased significantly [33,34]. By extracting resources, building infrastructure, and transforming natural habitats into productive lands, humans exert pressure on ecosystems. For instance, many species' habitats have been invaded by rapid urban expansion, resulting in a reduction of habitat and biodiversity for these species [35]. The projected increase in anthropogenic pressures in the future may cause species to leave their natural habitats, leading to severe population decline [36]. Rapid advances in remote sensing technology can more effectively quantify human pressures on habitats, measure the level of human activity by building a framework that considers a variety of human stresses, generate human footprint maps that provide an up-to-date picture of the extent of human activity on global terrestrial land, and describe the extent of the human alteration of ecosystems [37,38].

The unique geographical location and topography of Inner Mongolia has created a complex and diverse ecosystem that is one of the most complete natural ecosystem areas in China and a key area for biodiversity conservation. Previous studies on the identification of biodiversity hotspots have mostly been based on species richness and rarity, as well as on species distribution patterns; however, in general, species-based biodiversity hotspots still lack sufficient information to support them. This study combines remote sensing monitoring technology with the use of indices to identify biodiversity conservation hotspots; this process does not require a large amount of species data and has the advantages of shortening the process of assessment, expanding the scale, and saving the consumption of manpower, etc. The results of the analyses will allow for the development of comprehensive surveys of the biodiversity of hotspot areas and the dynamic monitoring of the hotspot in the long term.

In summary, long timeseries remote sensing observation data provide important data support for the study of the impacts of climate change and human activities on biodiversity [39,40]. This paper proposes a methodology for identifying biodiversity conservation hotspots by combining spatial–temporal remote sensing and human footprint indices. The main contributions of this study are as follows: (1) generating spatial–temporal

remote sensing indices to capture interannual and spatial variability in EVI and LST to quantify the impacts of climate change on biodiversity, (2) generating the human footprint index to quantify the impacts of human activities on biodiversity, and (3) integrating spatial-temporal remote sensing and human footprint indices to identify areas of high, medium, and low biodiversity conservation concern.

## 2. Study Area

The Inner Mongolia Autonomous Region is located in the northern part of China ( $37^{\circ}24'–53^{\circ}23'$  N and  $97^{\circ}12'–126^{\circ}4'$  E). It is the third largest provincial administrative division in China, with an area of nearly 10,000 km<sup>2</sup>. The area extends from the Daxingan Mountains in the east to the coast of the Guyan River in the west and diagonally from the northeast to the southwest in a long and narrow shape. The area is rich in vegetation, with forests, grasslands, and deserts along the northeast–southwest sequence. Most areas receive less than 500 mm of annual precipitation and are ecologically fragile, making them one of the most sensitive regions to global climate change. There are 11 ecological zones in the Inner Mongolia Autonomous Region, including plateau, forest, desert, and grassland. Considering that the geomorphological, hydrological, soil, vegetation, and climatic characteristics are relatively similar in each ecoregion, the ecological zones were chosen as the scale of analysis for this study (Figure 1).

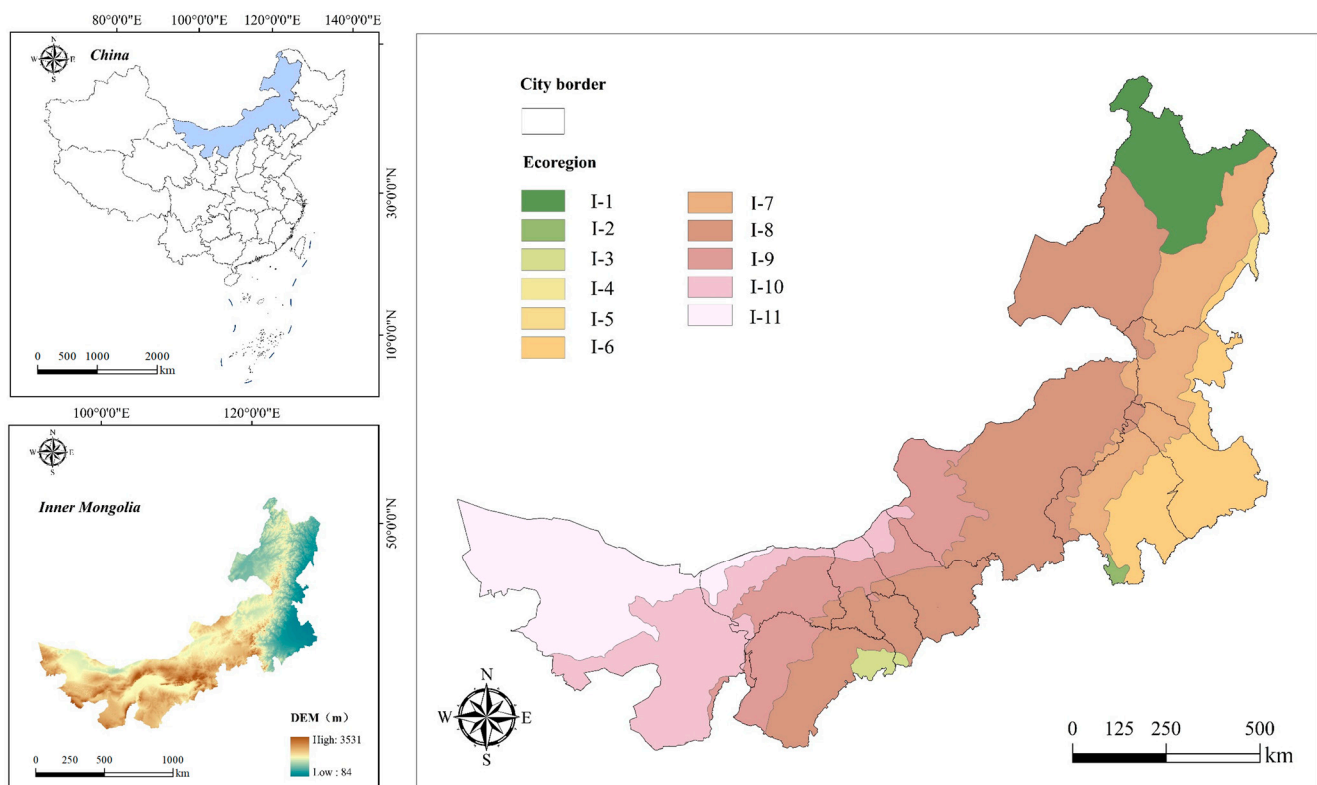


**Figure 1.** Overview map of the study area and main ecological zones (I-1 Northern Deciduous Coniferous Forest Ecoregion of the Daxingan Mountains; I-2 Yanshan–Taihang Mountains Deciduous Broadleaf Forest Ecoregion; I-3 Loess Plateau Agricultural and Grassland Ecological Zone; I-4 Mixed coniferous forest ecological zone in the Xiaoxinganling Mountains; I-5 Eastern Northeast Plain Agroecological Zone; I-6 Northeast Plain Western Meadow Grassland Ecoregion; I-7 Deciduous broad-leaved forest and forest-steppe ecotone in the southern–central Daxingan Mountains; I-8 Typical grassland ecological zone in the eastern–central part of Inner Mongolia Plateau; I-9 Longzhong Desert Grassland Ecoregion in Central Inner Mongolia Plateau; I-10 Longzhong Desert Grassland Ecoregion in Central Inner Mongolia Plateau; I-11 Grassland Desert Ecoregion in Central Inner Mongolia Plateau).

### 3. Research Methodology

In this study, MODIS multi-temporal remote sensing image data were used to obtain annual phenological and seasonal indicators of EVI and LST by fitting curves to generate interannual variability indices, whereas Landsat 8 standard deviation images were calculated to generate spatial variability indices. In addition, a human footprint index was calculated to generate a human footprint map of Inner Mongolia and quantify the impact of human activities on the ecosystem. The spatial–temporal remote sensing index (ST) and human footprint index (HF) were integrated to identify areas for conservation that are under climate change and anthropogenic pressures to finally obtain hotspot areas for biodiversity conservation in Inner Mongolia (Figure 2).

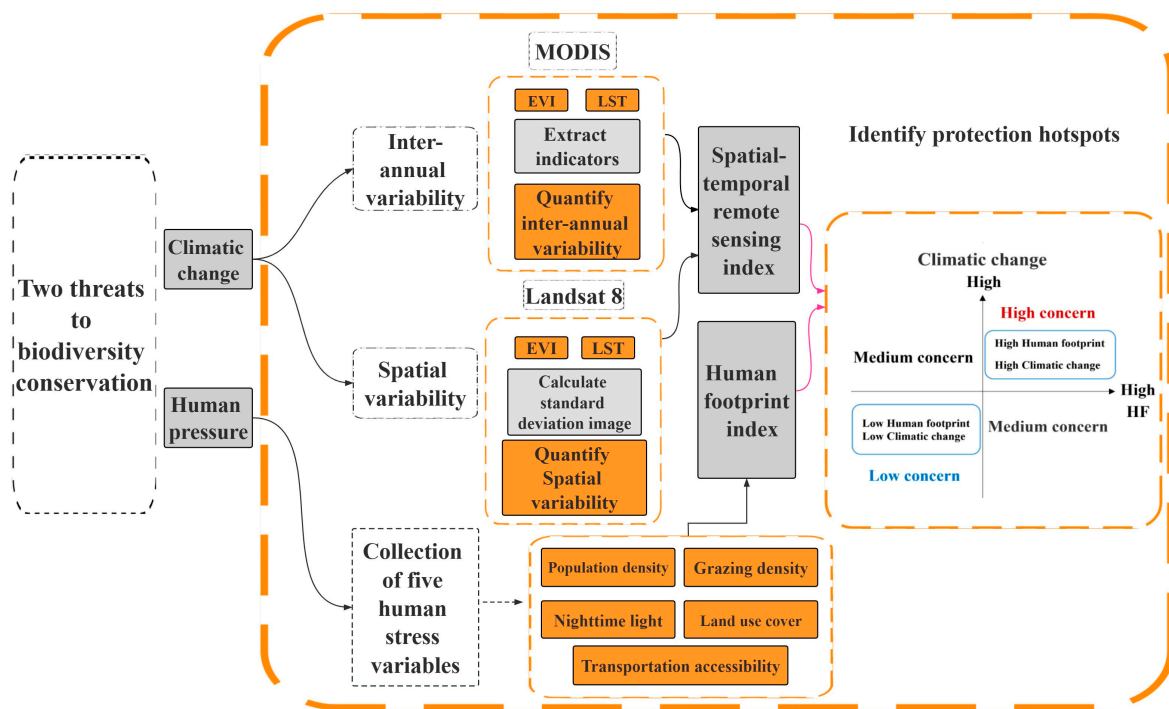


Figure 2. Overview of process.

#### 3.1. Identify Protection Hotspot Areas

In this study, the spatial–temporal remote sensing index (ST) and human footprint index (HF) were developed to identify biodiversity conservation hotspots based on two factors: climate change and human activities.

The analysis was based on the upper and lower quantiles of the spatial–temporal remote sensing index and human activity index maps. Hotspots were mapped using the Getis–Ord  $G_i^*$  statistic to identify pixel clusters in the categories of high and low conservation concern due to climate change and human activity [41].  $G_i^*$  is a local spatial autocorrelation indicator based on the full matrix of distances that can identify the locations in the study area where elements are highly concentrated, as follows:

$$G_{i_{ST}}^* = \frac{\sum_{j=1}^n w_{i_{ST},j_{ST}} x_{j_{ST}}}{\sum_{j=1}^n x_{j_{ST}}} \quad (1)$$

$$G_{i_{HF}}^* = \frac{\sum_{j=1}^n w_{i_{HF},j_{HF}} x_{j_{HF}}}{\sum_{j=1}^n x_{j_{HF}}} \quad (2)$$

In the formula,  $x_{j_{ST}}$  and  $x_{j_{HF}}$  are the attribute values of the elements  $j_{ST}$  and  $j_{HF}$ ,  $w_{i_{ST},j_{ST}}$  and  $w_{i_{HF},j_{HF}}$  are the spatial weights between the elements  $i_{ST}$  and  $j_{ST}$  and the elements  $i_{HF}$  and  $j_{HF}$ , and  $n$  is the total number of features.  $G_i^*$  statistics returned a z-score for each feature in the dataset. Hotspots were indicated by large positive z-score values and chilled



spots were indicated by large negative z-score values, identifying hot- and cold-spot areas with 99% confidence intervals.

By superimposing the two indices, a map of biodiversity conservation hotspots was calculated using the following formula:

$$BI\_G_i^* = G_{i\_ST}^* \oplus G_{i\_HF}^* \quad (3)$$

where  $BI\_G_i^*$  is the biodiversity conservation hotspot identified by combining the two indices,  $G_{i\_ST}^*$  is the hotspot area identified by the ST index and  $G_{i\_HF}^*$  is the hotspot area identified by the HF index.  $\oplus$  is calculated as the part of the area where two hotspots overlap, i.e., the area where both indices have significantly high values, and is classified as “Level 1” protected areas; areas without overlap, i.e., areas where either of the two indices have a significantly higher value, are classified as “Level 2” protected areas; and areas with low values for either of the two indices are classified as “Level 3” protected areas. The final biodiversity conservation hotspot area  $BI\_G_i^*$  is classified as a three-tier priority conservation area.

### 3.2. Constructing ST Index for Identifying Hotspot Areas

Climate change can lead to seasonal changes in vegetation phenology and temperature, resulting in a phenological mismatch between the species and the resources on which they depend for survival, reproduction, and habitat characteristics. In this study, we used MODIS multi-temporal remote sensing image data to obtain EVI and LST annual phenology and seasonal indicators by fitting curves to generate interannual variability indices. Landsat 8 standard deviation images were used to generate a spatial variability index. To obtain the spatial–temporal patterns of the EVI and LST, we integrated the interannual and spatial variability indices.

Based on the quantile method used to classify each index into high and low values, the spatial–temporal maps of EVI and LST were integrated as follows: (1) interannual variability of EVI (MODIS 16-day EVI; 250 m resolution) and spatial variability with EVI (Landsat 8 EVI standard deviation; 30 m resolution) and (2) interannual variability of LST (MODIS 8-day LST; 1 km resolution) and spatial variability with LST (Landsat 8 LST standard deviation; 30 m resolution). Prior to integration, resampling was performed using nearest neighbor resampling to produce two spatial–temporal variation maps: an EVI spatial–temporal map at 250 m resolution and a LST spatial–temporal map at 1 km resolution.

Finally, we combined the interannual variability maps of the EVI and LST with their respective spatial variability maps (Table 1). Based on the principle of spatial coherence, hotspots of biodiversity conservation due to phenological and seasonal variability were identified by combining the interannual and spatial variability indices.

**Table 1.** Identification of biodiversity conservation hotspots due to phenological and seasonal variability.

	High Spatial Variability	Low Spatial Variability
High interannual variability	Medium conservation (high interannual variability poses a high threat but high spatial variability in EVI and LST implies high resilience)	Highest conservation (high interannual variability poses high threat; low spatial variability in EVI and LST means low resilience and low elasticity)
Low interannual variability	Lowest conservation (low interannual variability poses low threat level; high spatial variability in EVI and LST implies high resilience)	Medium conservation (low interannual variability poses low threat level; low spatial variability in EVI and LST implies low resilience)

#### 3.2.1. Interannual Variability Index

First, MODIS images of the EVI and LST of the Inner Mongolia region from 2002 to 2022 were acquired from the Google Earth Engine and the best-quality cloud-free data were

selected according to the MODIS quality control (QA) bands. The 20-year EVI and LST timeseries were filtered using the adaptive Savitzky–Golay filter of TIMESAT software and, based on the curves obtained from the timeseries, the three phenological indices (EVI) and three seasonal indices (LST) were calculated for each year; the start of the growing season (SOS), end of growing season (EOS), and length of growing season (LOS) were determined using the dynamic threshold method (Table 2). To determine the accuracy of the metrics, this study examined the accuracy of SOS and EOS identified by different models using the phenological observation data released by the China National Ecosystem Observation and Research Network. Based on the latitude and longitude of the observation points and the year of the phenological data, the mean values of the  $3 \times 3$  pixels were extracted from the simulated raster data and compared with the measured data and the correlation coefficient and root mean square error were calculated. Finally, to quantify the interannual variation, the coefficient of variation (CV) was calculated for each of the six indicators; the CV is a statistical measure of the dispersion of serial observations and can reflect the temporal differences in phenology at the pixel level for any land cover type, calculated as:

$$T_{CV} = \frac{STD}{\mu} \quad (4)$$

where  $T_{CV}$  denotes the interannual variability index,  $STD$  denotes the standard deviation, and  $\mu$  denotes the arithmetic mean.

**Table 2.** Phenology and seasonal indicators and interannual variability indices.

Phenology and Seasonal Indicators	Description	Interannual Variability Index
$E_{sos}$	Start of the growing season based on EVI timeseries	$T_{CV\_E_s}$
$E_{eos}$	End of the growing season calculated from EVI timeseries	$T_{CV\_E_e}$
$E_{los}$	Number of days between EVI start date and end date	$T_{CV\_E_l}$
$L_{sos}$	Start of the growing season based on LST timeseries	$T_{CV\_L_s}$
$L_{eos}$	End of the growing season calculated from LST timeseries	$T_{CV\_L_e}$
$L_{los}$	Number of days between LST start date and end date	$T_{CV\_L_l}$

To test whether the physical and seasonal indices were correlated, Pearson correlation coefficients ( $r$ ) were calculated between the three EVI and three LST interannual variability indices to determine whether it was meaningful to retain all indices and select the most closely related seasonal indices for further analysis based on principal component analysis.

### 3.2.2. Spatial Variability Index

The spatial variability of EVI and LST was obtained by calculating the standard deviation images of Landsat 8 EVI and LST in the Inner Mongolia region from 2013 to 2022 on the Google Earth Engine by analyzing their image textures.

Landsat 8 surface reflectance layer 1 bands 2, 3, and 4 were used to determine the EVI. To obtain the highest quality images, the images were first masked for clouds, shadows, and water bodies using quality assurance (QA) bands from Landsat 8. Second, by calculating the 90th percentile of EVI values for each year from 2013 through 2022, synthetic images were created. The 90th percentile is a ranking of the values by their size, dividing the data into the lower 90% and the upper 10% and discarding the data in excess of 10%, which eliminates erroneous high EVI values [29]. The spatial variability index of the EVI was obtained by employing an  $11 \times 11$  pixel moving window to determine the standard deviation of 90% of the EVI images. The 90th percentile of the EVI of the neighboring pixels was used to calculate the standard deviation for the moving window's center pixel. A window size of  $11 \times 11$  was chosen because an ecologically significant window of 330 m

represents a refuge within a region accessible to most species. The formula for calculating the spatial variability index of the EVI is as follows:

$$S_{STD\_EVI} = \sqrt{\frac{\sum_{i=1}^n (x_i - \mu)^2}{n}} \quad (5)$$

where  $S_{STD\_EVI}$  denotes the spatial variability index of the EVI,  $\mu$  is the arithmetic mean, and  $n$  is the sample.

The LST was calculated from Landsat 8-band10 by first collecting images of the Inner Mongolia region in summer (June–August) and winter (December–February) for each year from 2013 to 2022 and obtaining median synthetic images of the summer and winter for all years. The median was analyzed because it minimized the effects of extreme values in the data [25]. Standard deviations were calculated within a moving window of  $11 \times 11$  pixels for summer and winter based on median synthetic images for both summer and winter, as they are the extreme high and low temperatures, respectively, that affect biodiversity patterns [25,42]. To determine the spatial variability of the LST, the LST spatial variability index  $S_{STD\_LST}$  was generated by combining the summer and winter data. Standard deviation images for the summer and winter seasons were quantile-classified into five categories, ranging from 1 (low standard deviation, low variability) to 5 (high standard deviation, high variability). Combining all the possibilities generated by classifying images with two standard deviations for summer and winter resulted in yield values ranging from 2 to 10 (Figure 6). Finally, locations with high spatial variability in both summer and winter were classified as having high spatial variability (combined sum  $\geq 7$ ), whereas regions with low spatial variability in both summer and winter were classified as having low spatial variability (combined sum range 2–6). The formula for calculating the spatial variation index of the LST is as follows:

$$S_{STD\_LST} = \sqrt{\frac{\sum_{i=1}^n (x_i - \mu)^2}{n}} \quad (6)$$

where  $S_{STD\_LST}$  denotes the spatial variability index of the EVI,  $\mu$  is the arithmetic mean, and  $n$  is the sample.

### 3.3. Construction of Human Footprint Index for Identifying Hotspot Areas

The *HF* index is used to indirectly assess the impacts associated with human activities by integrating a range of human pressures into a framework in which the relative levels of pressure are aggregated [43]. Five human activity factors, namely population density, livestock density, land use, nighttime light index, and transportation, were selected to quantify human disturbances in terrestrial ecosystems by mapping human footprints at a spatial resolution of 1 km to determine the *HF* in Inner Mongolia while considering the actual conditions of the region. The impact of human activity increased with increasing *HF* values. Data related to population density, livestock density, land use, nighttime light index, and accessibility were assigned values ranging from 1 to 10 and superimposed to obtain the *HF*.

$$HF = \frac{HII - HII_{\min}}{HII_{\max} - HII_{\min}} \quad (7)$$

where *HF* is the human footprint and *HII* is the human impact index.  $HII_{\max}$  and  $HII_{\min}$  are the maximum and minimum values of the human impact index, respectively. The calculation method is as follows:

$$HII = \text{population} + \text{grazing} + \text{nightlight} + \text{transportation} + \text{landuse} \quad (8)$$

where *population* is population density, *grazing* is grazing density, *nightlight* is nighttime light, *transportation* is the traffic impact index, and *landuse* is land use.

### 3.3.1. Population

Population density is a key determinant of population spatial distribution. This study used the latest raster data on the population spatial distribution in 2021 that was published by Landsat (<https://landscan.ornl.gov>) (accessed on 1 May 2023). The effect of population density on the ecosystem is logarithmic [44], putting the population density data into a logarithmic equation and using the natural breakpoint method to classify the data into 10 classes with a value range of 0–10.

$$population_{score} = 2.21398 \times \log(population_{density} + 1) \quad (9)$$

In the formula,  $population_{score}$  represents the reallocated grid score and  $population_{density}$  represents the grid's population density value.

### 3.3.2. Grazing

Livestock density data were obtained from the World Gridded Livestock Dataset of the United Nations Food and Agriculture Organization (<https://data.apps.fao.org>) (accessed on 1 May 2023).

Livestock grazing is an important industry in Inner Mongolia and an important type of human activity in this region. In this study, the sum of the cattle and sheep densities was used to characterize the grazing density. Because the world gridded livestock dataset only obtained cattle and sheep densities in 2016, in order to obtain the grazing density in 2021 we needed to analyze the trend extrapolation method for cattle and sheep density in 2016 before reassigning the value [45]. First, the total beef and lamb production values in the Inner Mongolia Autonomous Region in 2015, 2016, and 2021 were obtained from the statistical yearbook, the change rate of beef and lamb production in 2021 relative to the production in 2016 was calculated, and the cattle and sheep density in 2021 was obtained by multiplying the change rate with the cattle and sheep density in 2016 to obtain the final grazing density. The data for grazing density were also calculated and allocated using the logarithmic equation with a value range of 0–10 points, since the effect of grazing density also showed a logarithmic variation law; the specific calculation equation was as follows:

$$grazing_{score} = 2.51531 \times \log(grazing_{density} + 1) \quad (10)$$

In the formula,  $grazing_{score}$  stands for the reallocated grid score and  $grazing_{density}$  stands for the grid's grazing density value.

### 3.3.3. Nightlight

The nighttime lighting index is used to indicate the level of human activity at night, which also reflects the level of economic development and the creation of electrical infrastructure. Data were obtained from the DMSP-OLS timeseries data for China from 1992 to 2019 [46]. The data were calibrated to the DMSP-OLS data and the consistency of the temporal resolutions of the DMSP-OLS and SNPP-VIIRS data was considered with a spatial resolution of 1 km. The data were scaled to 0–10 points using the quantile method.

### 3.3.4. Transportation

Transportation was determined using the road and rail data from Inner Mongolia. The road network data were obtained from OpenStreetMap (<https://www.openstreetmap.org/>) (accessed on 1 May 2023). The environmental impact of roads was studied by assigning scores to roads and railroads [45,47]. Because the train is closed when it runs along the railroad, the influence on both sides is small; therefore, when evaluating the value, only the area within 2500 m on both sides of the railroad was assigned nine points, within 2500–3000 m was assigned five points, and within 3000–5000 m was assigned three points. The highway was assigned ten points within 500 m, within 500–2500 m it was assigned eight points, within 2500–3000 m it was assigned seven points, and within 3000–5000 m

it was assigned three points. An area within 500 m on both sides of the road was worth 10 points, within 500–2500 m was worth 8 points, within 2500–3000 m was worth 7 points, and within 3000–5000 m was worth 5 points. The road and railroad buffers were mosaicked into a new grid and the maximum values of railroad and road overlap were obtained to assess the accessibility of traffic lanes.

### 3.3.5. Land Use

Land use is an important indicator of the intensity of human activities. Based on the relative degree of disturbance calculated in a regional-scale correlation study [48], a score was assigned to each land use type. We assigned building land, which is the land use type most affected by human activities, a maximum score of 10, whereas all other land use types that were not significantly affected by human activities were assigned a value of 0. Finally, built-up land, cropland, grassland, watershed, forest land, and unused land were assigned values of 10, 2, 0, 0, 0, 0, and 0, respectively.

These data are a 10 m resolution global land cover map for 2021 (<https://www.esri.com/>) (accessed on 1 May 2023) that was produced using the Sentinel-2 satellite as the data source combined with an artificial intelligence land classification model.

## 4. Results

### 4.1. Spatial–Temporal Remote Sensing Indices to Identify Conservation Areas Affected by Phenological and Seasonal Changes $G_{i\_ST}^*$

#### 4.1.1. Interannual Variability of MODIS EVI and LST

Assessment of the interannual variation of the EVI in Inner Mongolia was based on the CV of three phenological indicators: SOS, EOS, and LOS ( $T_{CV\_E_s}$ ;  $T_{CV\_E_e}$ ;  $T_{CV\_E_l}$ ). These three indicators had Pearson correlations between 0.72 and 0.84, indicating a moderate-to-high degree of correlation. The most correlated  $T_{CV\_E_s}$  was selected using principal component analysis to further analyze the interannual variation of the EVI. The values of  $T_{CV\_E_s}$  varied greatly throughout Inner Mongolia, reaching  $>0.4$  in some locations of the typical grassland ecoregion in the easternmost Inner Mongolia Plateau (Figure 3a) and higher  $T_{CV\_E_s}$  values ( $CV > 0.25$ ) in most of the typical grassland ecoregion in the central–eastern Inner Mongolia Plateau, the meadow grassland ecoregion in the western Northeast Plain, and the grassland-dominated eastern Hulunbuir City and western Xilin Gol League.  $T_{CV\_E_e}$  was lower (mean  $CV < 0.15$ ) in the mountainous desert ecoregion of the western Inner Mongolia Plateau, the steppe desert ecoregion of the central Inner Mongolia Plateau, the Longzhong desert steppe ecoregion of the central Inner Mongolia Plateau, and the desert dominated Alxa League. Unlike the strong interannual variation at the beginning of the growing season, the interannual variation at the end of the growing season was small and the  $T_{CV\_E_e}$  values (Figure 3b) were low throughout Inner Mongolia. The  $T_{CV\_E_l}$  (Figure 3c) was approximately the same as the  $T_{CV\_E_e}$ .

Similarly, the interannual variation of the LST in Inner Mongolia was assessed based on the CV of the three indicators, SOS, EOS, and LOS ( $T_{CV\_L_s}$ ;  $T_{CV\_L_e}$ ;  $T_{CV\_L_l}$ ). The three surface temperature indices were moderately highly correlated, with Pearson correlations ranging from 0.53 to 0.82. The most relevant  $T_{CV\_L_s}$  was selected as the interannual variation index of the LST. The overall variation in  $T_{CV\_L_s}$  was small, with a maximum CV of 0.31, and  $T_{CV\_L_s}$  was significantly higher than  $T_{CV\_L_e}$  (Figure 4a,b). The highest  $T_{CV\_L_l}$  variability (mean  $CV > 0.15$ ) was found in the deciduous broad-leaved forest and forest-steppe ecotone in the southern–central Daxinganling and the meadow ecotone in the western Northeast Plain, whereas the lowest variability was found in the mountainous desert ecotone in the western Inner Mongolia Plateau, Central Inner Mongolia grassland desert ecoregion, and the Longzhong desert grassland ecological zone in Central Inner Mongolia. Additionally,  $T_{CV\_L_e}$  and  $T_{CV\_L_l}$  were not significantly different across the autonomous region ( $CV < 0.1$ ; Figure 4b,c).



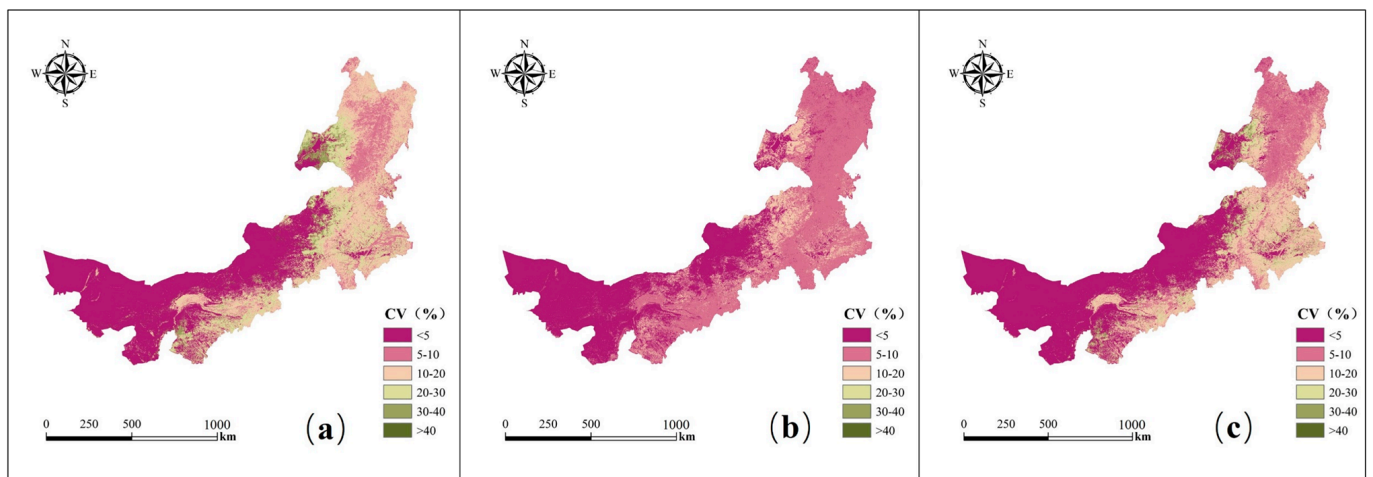


**Figure 3.** (a) EVI coefficient of variation  $T_{CV\_Es}$ ; (b) EVI coefficient of variation  $T_{CV\_Ec}$ ; (c) EVI coefficient of variation  $T_{CV\_El}$ .

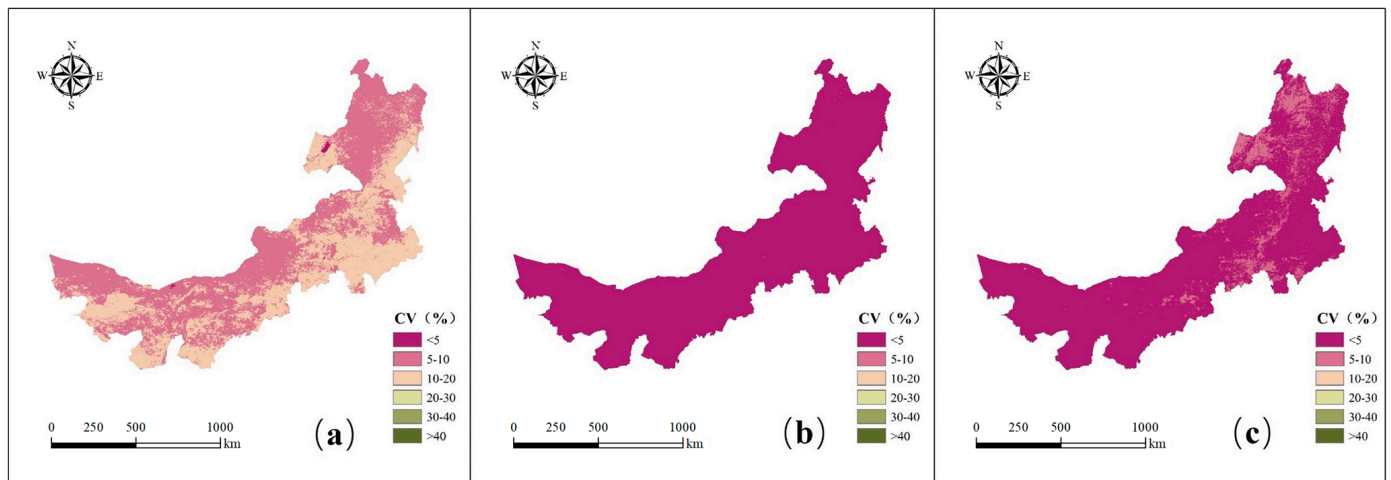


**Figure 4.** (a) LST coefficient of variation  $T_{CV\_Ls}$ ; (b) LST coefficient of variation  $T_{CV\_Lc}$ ; (c) LST coefficient of variation  $T_{CV\_Ll}$ .

Comparing the interannual variability indices of EVI and LST in Inner Mongolia, it was found that the correlation between them was weak; the areas with high interannual variability in EVI were not the same as those with high interannual variability in LST. Specifically,  $T_{CV\_Es}$  and  $T_{CV\_Ls}$  were weakly positively correlated across Inner Mongolia ( $r = 0.11$ ); however, they varied between ecoregions and municipalities.

#### 4.1.2. Spatial Variability of Landsat 8 EVI and LST Standard Deviation Image Textures

The spatial variability of the EVI in Inner Mongolia was assessed by calculating the standard deviation of the Landsat 8 EVI in an  $11 \times 11$  pixel moving window. The highest spatial variability in the EVI was found in ecoregions dominated by forest, grassland, and agricultural land cover types, such as the deciduous coniferous forest ecoregion in the northern part of the Daxinganling Mountains, the deciduous broad-leaved forest and forest-steppe ecoregion in the southern-central part, the meadow ecoregion in the western part of the Northeast Plain, and the eastern part of the typical grassland ecoregion in the eastern-central part of the Inner Mongolia Plateau. Within each ecoregion of Inner Mongolia, the spatial variability of the EVI varied greatly between the same land cover class and different land cover types. For example, the spatial variability was higher in the meadow-steppe and agroecological zones in the western part of the forest-dominated

Song Nen Plain near impervious surfaces and farmland (Figure 5(1a–c)). In the farmland-dominated Hetao-Yinchuan irrigated agroecological zone, farmland and grassland showed high spatial variability (Figure 5(2a–c)). In the grassland-dominated Xilin Gol League typical grassland ecoregion, the spatial variability of the EVI was higher when the distance to bare land and farmland was smaller (Figure 5(3a–c)). In the desert ecoregion of northern Alxa, which is dominated by bare land (Figure 5(4a–c)), the standard deviation of the EVI could capture the fine-scale variability of land cover classes. Among the ecoregions, the spatial variability of vegetation greenness was highest in the Yanshan–Taihang Mountains deciduous broad-leaved forest ecoregion, the western Northeast Plain meadow-steppe ecoregion, and the eastern Northeast Plain agricultural ecoregion (mean > 0.1) and lowest in the western Inner Mongolia Plateau, the northern mountain desert ecoregion, and the central steppe desert ecoregion (mean < 0.03). Among the cities, the spatial variability of the EVI was highest in Hohhot and Chifeng (mean > 0.09), and the spatial variability of vegetation greenness was lowest in the Alxa League and Bayan Nur (mean < 0.04).

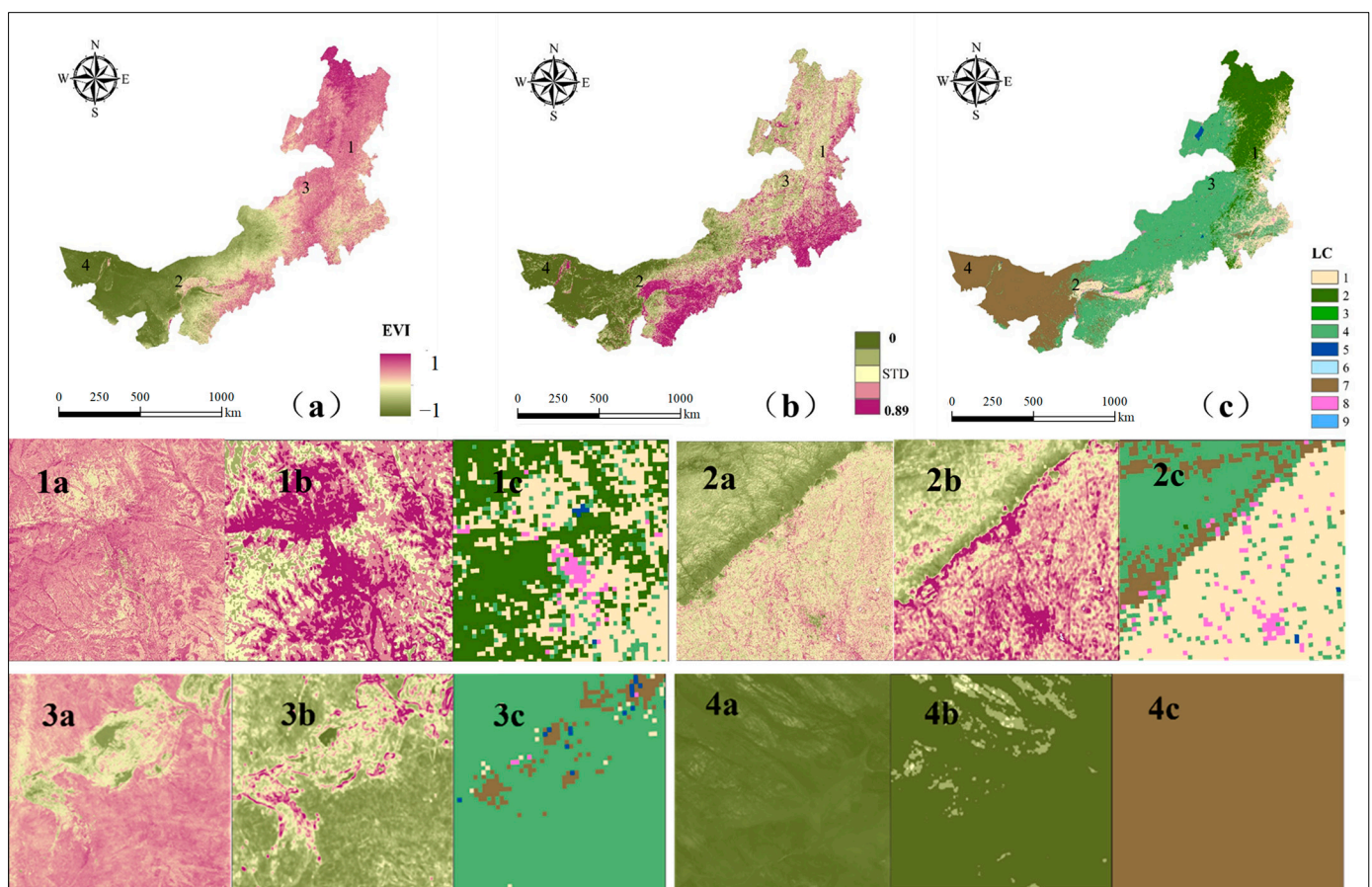


**Figure 5.** (a) Enhanced vegetation index (EVI), (b)  $S_{STD\_EVI}$ , and (c) land cover map with the following categories: 1. Agricultural land 2. Forest 3. Shrubs 4. Grassland 5. Watershed 6. Snow and ice 7. Bare ground 8. Impervious surface 9. Wetlands. Numbers 1–4 indicate the location of insets on the map.

The southwest of Inner Mongolia is where the LST is concentrated throughout the summer, whereas during winter, the LST diminishes from south to north (Figure 6a,b). This was combined with the spatial variability of surface temperatures in the summer and winter (Figure 6(3c)).

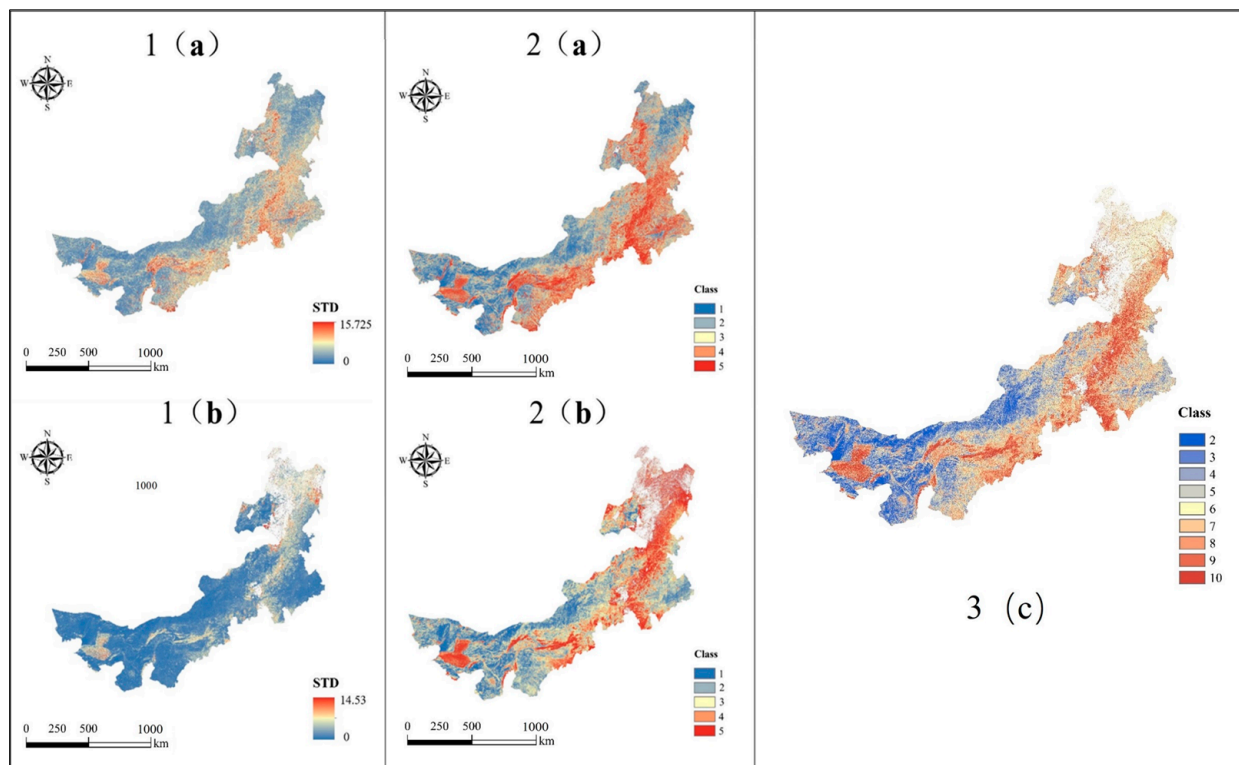


**Figure 6.** (a) Summer LST median. (b) Winter LST median. (1a) Spatial variability of summer LST; (1b) spatial variability of winter LST; (2a) Summer LST spatial variability classification; (2b) Winter LST spatial variability classification; (3c)  $S_{STD\_LST}$  (spatial variability index of LST: combining summer and winter).

#### 4.1.3. Spatial–Temporal Remote Sensing Index Patterns of the EVI and LST

The interannual variability maps of EVI and LST in Inner Mongolia (Figure 7(1a,2a)) and their spatial variability maps (Figure 7(1b,2b)) were analyzed according to the combination of their respective high and low variabilities (Table 1) to pinpoint locations whose phenological and seasonal variability could create high, medium, and low conservation concerns (Figure 7(1c,2c)). Pixel clustering was used to identify protection hotspots based on the EVI and LST, which differed significantly (Figure 7(1d,2d)). The conservation hotspots identified based on the EVI (Figure 7(1d)) were mainly concentrated in the Deciduous broad-leaved forest and grassland forest ecotone in the southern–central Daxingan Mountains and the typical grassland ecological zone in the eastern–central Inner Mongolia Plateau, whereas the hotspots identified based on the LST were concentrated in the southern–central meadow and grassland ecological zone in the west of the Northeast Plain and the south of the typical grassland ecological zone in the eastern–central Inner Mongolia Plateau and the municipal levels were mainly concentrated in the east of Hulunbuir City, the east and south of Chifeng City, the south of Xilin Gol League, and the southwest of Ulanqab. The spatial–temporal remote sensing index were used to identify conservation hotspot areas  $G_{i\_ST}^*$  due to phenological and seasonal changes and were mainly distributed in eastern Hulunbuir City, eastern Hinggan League, eastern Chifeng City, and southern Xilin Gol League based on the spatial consistency between the EVI and LST (Figure 7(3d)).



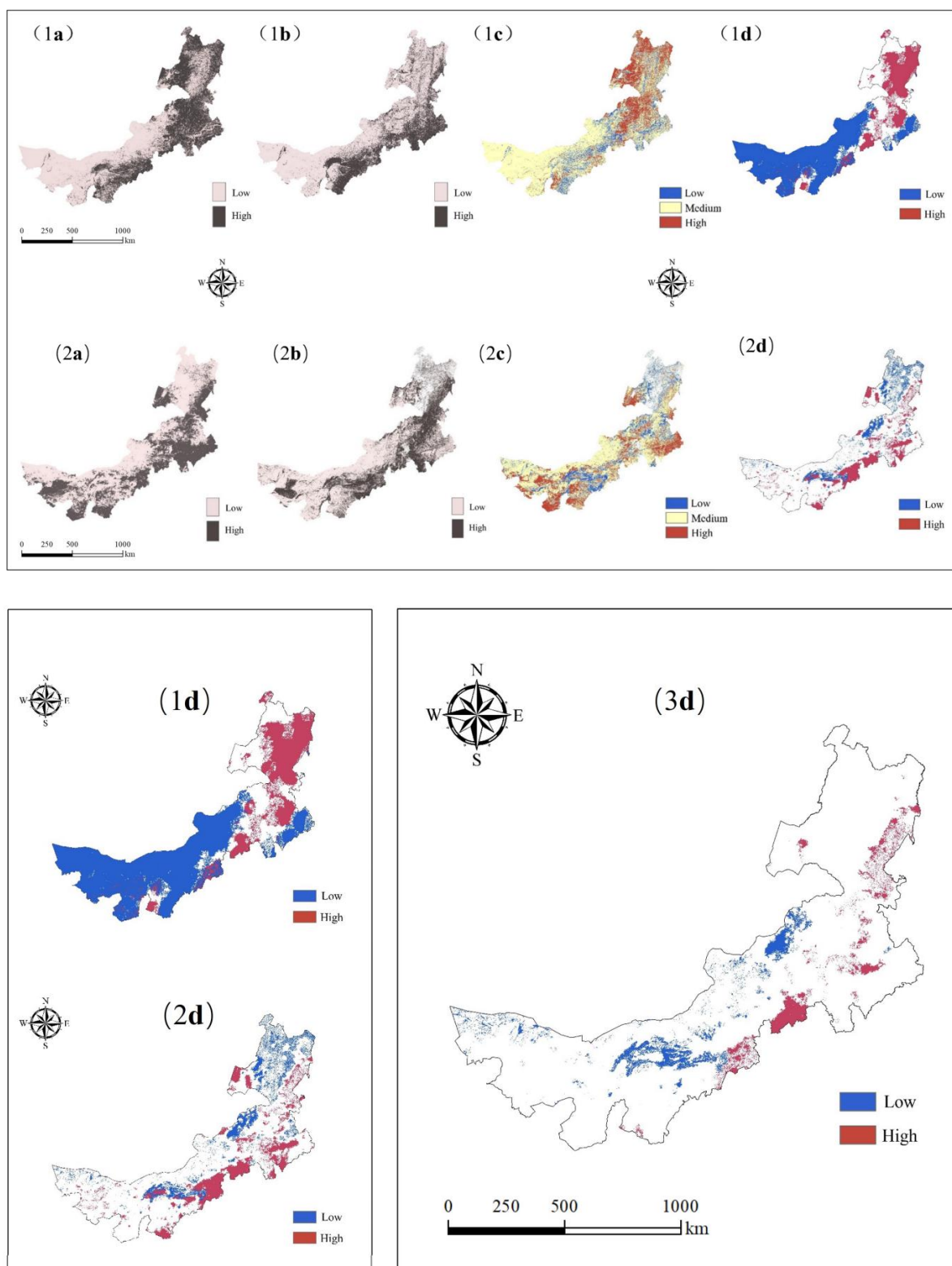


**Figure 7.** (a) High and low interannual variability of EVI. (1b) High and low spatial variability of EVI. (1c) Integration of EVI interannual and spatial variability. (1d) Hotspots for EVI identification. (2a) High and low LST interannual variability. (2b) High and low LST spatial variability. (2c) Integration of LST interannual and spatial variability. (2d) Hotspots identified by LST. (3d) Spatial-temporal remote sensing index to identify protection hotspot areas  $G_{i\_ST}^*$ .

## 4.2. Human Footprint Index Identifies Conservation Hotspots Affected by Anthropogenic Activities $G_{i-HF}^*$

### 4.2.1. Spatial Distribution of Each Human Activity Factor

Five types of human activity factors were selected, considering the actual situation in Inner Mongolia: population density, grazing density, land use data, night illumination index, and traffic accessibility (Figure 8).

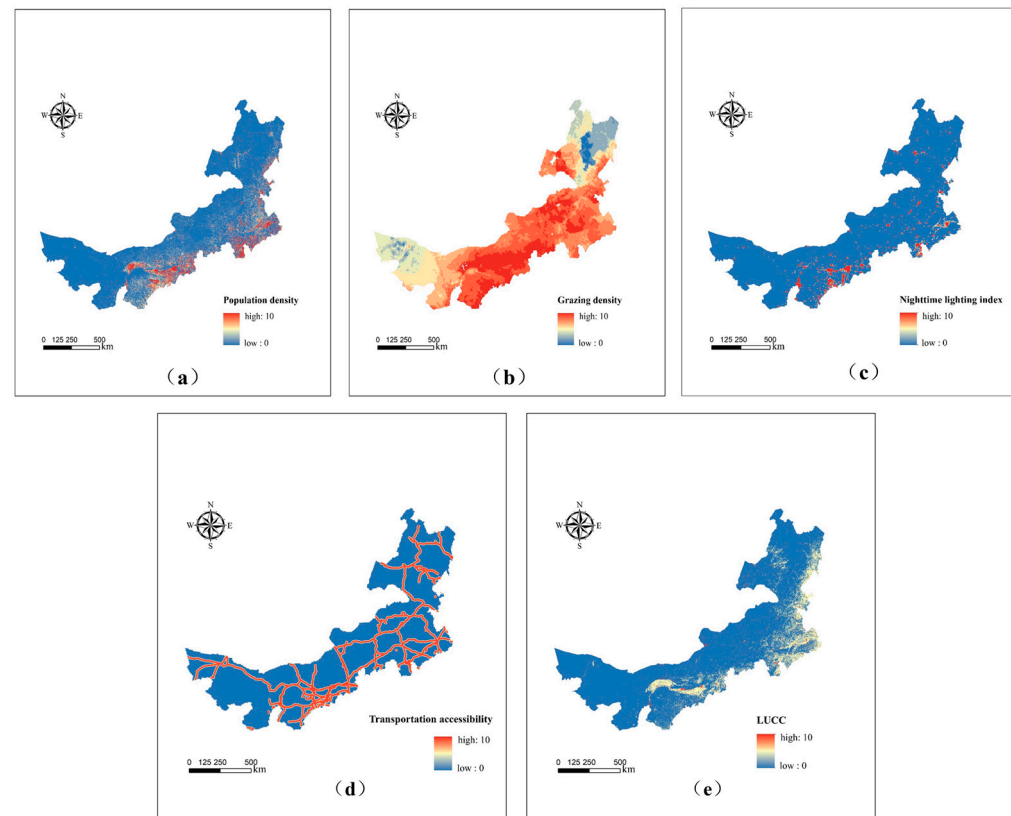


**Figure 8.** Factors influencing human footprint in Inner Mongolia: (a) population density, (b) grazing density, (c) night lighting, (d) transportation accessibility, and (e) land use.

According to Figure 8a, the population in the Inner Mongolia Autonomous Region is distributed roughly along the line between the eastern foot of the Daxinganling Mountains, the Yinshan Mountains, and the Helan Mountains. The population density is lower from the north of this line to the west and higher from the east to the south. The population density varies significantly among allied cities. For example, Hohhot in the central region has a higher population density, whereas the Alxa League in the west has a lower population density due to economic development disparities.

Animal husbandry is a basic industry in Inner Mongolia, and grazing is an important human activity in this region. As shown in Figure 8b, the spatial distribution pattern of grazing density in the Inner Mongolia Autonomous Region was high in the central region and low in the western and northeastern regions. Areas with high grazing density included the central–eastern part of the Xilin Gol League, Bayan Nur City, Erdos City, eastern Chifeng City, and Tongliao City.

Nighttime lighting data are important indicators of the intensity of human activity. According to the nighttime light in Figure 8c, the spatial distribution of nighttime light in the Inner Mongolia Autonomous Region is uneven and is mainly distributed in cities along the mainstream of the Yellow River and along the traffic arteries. Due to the huge difference in urbanization levels between the eastern, central, and western parts of Inner Mongolia, the intensity of nighttime lighting and urbanization levels in the central part of the country are significantly higher than those in the eastern and western parts. The top three cities



in terms of total nighttime lighting value in each league are Hulunbuir City, Xilin Gol League, and Alxa League. There is a strong correlation between population density and nighttime lights in the Inner Mongolia region in terms of the spatial distribution because nighttime lights can accurately reflect the population gathering in urban areas where lights are concentrated.

The traffic impact index was based on road and railroad data from Inner Mongolia, and the intensity of human activity was determined by establishing buffer zones and assigning scores according to different distances (Figure 8d). The road network in Inner Mongolia has a significant concentration of cities at the prefecture level, whereas the railroad network has an axial pattern of town linkages owing to the “corridor effect” of the railroad, with the east–west railroad line as the axis for expansion. The core cities and important nodal towns in Inner Mongolia are clearly oriented with Hohhot as the axis, which connects with cities outside the province and radiates to the inner regions.

Land use in Inner Mongolia is dominated by grassland, forest land, and unused land, whereas water, arable land, and residential land occupy relatively small areas. Grassland is distributed in most of the central part of the country, unused land is in the western part, forested land is in the eastern part, arable land is on the southeastern border, and water and residential land are interspersed among the above land types. The high values were obtained mainly for the southeastern part of Inner Mongolia, where the land use types were mainly farmland and construction land, and the low values were mainly in the western desert areas (Figure 8e).

#### 4.2.2. Distribution Pattern of Human Footprint Index

The human footprint index was calculated by superimposing each human activity factor in Inner Mongolia, and the results are shown in Figure 9a. The HF was classified into three levels using the natural breakpoint method (Figure 9b): low (1–10), medium (10–20), and high (20–49). High HF values were distributed in urban construction areas, cultivated land, and road construction areas where the degree of human disturbance was high. Low values were distributed in undeveloped areas surrounded by deserts, forests, and grasslands, where the disturbance caused by human activities was low.

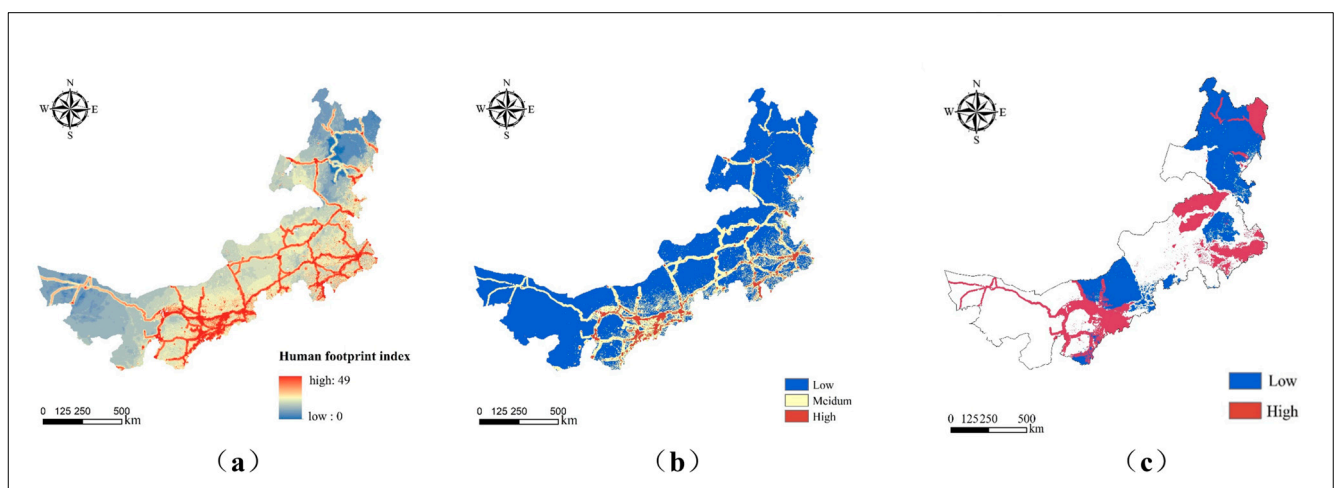


**Figure 9.** (a) HF index. (b) HF high and low classification. (c) HF-identified human activity hotspot map  $G_{i\_HF}^*$ .

For the identification of a human activity hotspot map  $G_{i\_HF}^*$  based on HF (Figure 9c), the hotspot areas of  $G_{i\_HF}^*$  mainly included: the West Liaoning River Plain, the southern side of the Daqing Mountains, the southeastern part of the Ordos Plateau, the northern foot of the Yinshan Mountains, the Daxinganling Mountains, the Helan Mountains, and the Hetao Plain. The population in these areas is mostly distributed along rivers or traffic routes, with a high population concentration, higher nighttime light intensity and high

urbanization levels compared with other areas, better traffic accessibility, and a higher intensity of human activities.

#### 4.3. Results of Hotspot Protection Zone Identification $BI\_G_i^*$

According to Equation (3),  $BI\_G_i^*$  was calculated to assess the degree of threat to biodiversity in the Inner Mongolia Autonomous Region from two dimensions, climate change and human activities (Table 3), and to further plan priority protected areas (Figure 10).

**Table 3.** Basis of priority conservation areas.

Priority Zone Level	Climate Change Threatening	Human Activities Threatening
Primary Protection Priority Area (A1–A12)	High	High
Secondary Protection Priority Area	High	Low
	Low	High
Tertiary Protection Priority Area	Low	Low

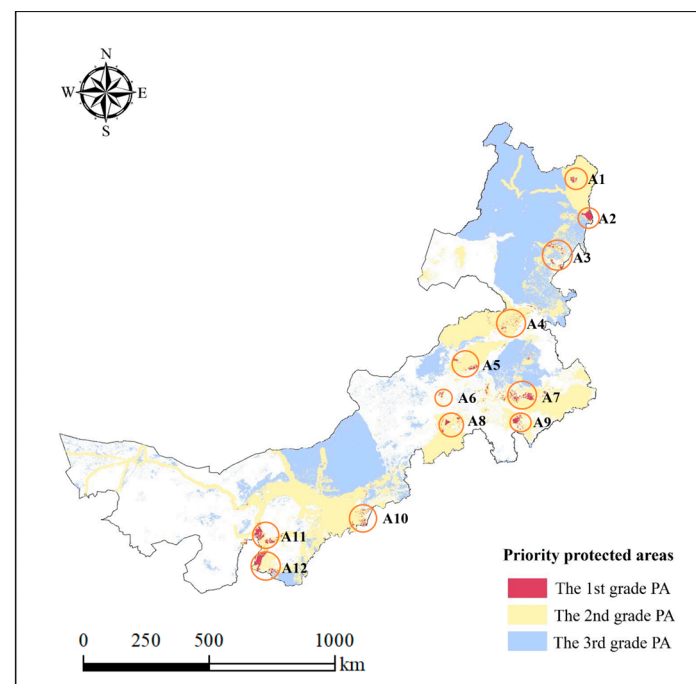


**Figure 10.** Combining spatial–temporal remote sensing and human footprint indices to delineate hotspot reserves.

#### Number, Area, and Spatial Distribution Characteristics of Priority Protected Areas $BI\_G_i^*$

The results show that the priority protection areas generated from the combination of the ST and HF indices in Inner Mongolia had a total area of 668,508 km<sup>2</sup> (Figure 11), of which, 10,581 km<sup>2</sup> were priority protection areas, accounting for 0.91% of the total land area of the Inner Mongolia Autonomous Region and 1.58% of the total area of priority protection areas. These areas were divided into 12 priority protection areas according to the topography of the main ecological zones and administrative divisions, some of which contained multiple protection zones (those indicated with (\*) in Table 4 are the existing protection zones). The primary protected areas are scattered and concentrated mainly in the eastern part of the country. The second priority protection area covers 273,641 km<sup>2</sup>, which is mainly distributed in the northeastern part of the Xinganling Mountains, coniferous forests, mixed coniferous and broad coniferous forest ecological zones, most areas in the western meadow grassland ecological zone of the Northeast Plain, the central and southern parts of the typical grassland ecological zone in the central–eastern part of the

Inner Mongolia Plateau, the agricultural and grassland ecological zone of the Loess Plateau, and the western part of the desert grassland ecological zone in the central Longzhong Inner Mongolia Plateau. The second level of priority protection zone is based on the areas with a significantly high value of any one of the two hotspot indices and accounts for 40.93% of the total area of the priority protection zone. The third level of priority protection zone covers 304,286 km<sup>2</sup> and accounts for 57.48% of the total area of the priority protection zone. This is the largest of the three types of priority protected areas and is mainly located in the northern Daxinganling mountain mixed coniferous forest ecological zone, the deciduous broad-leaved forest ecological zone in southern–central Daxinganling, and the grassland desert ecoregion in the Central Inner Mongolia Plateau.

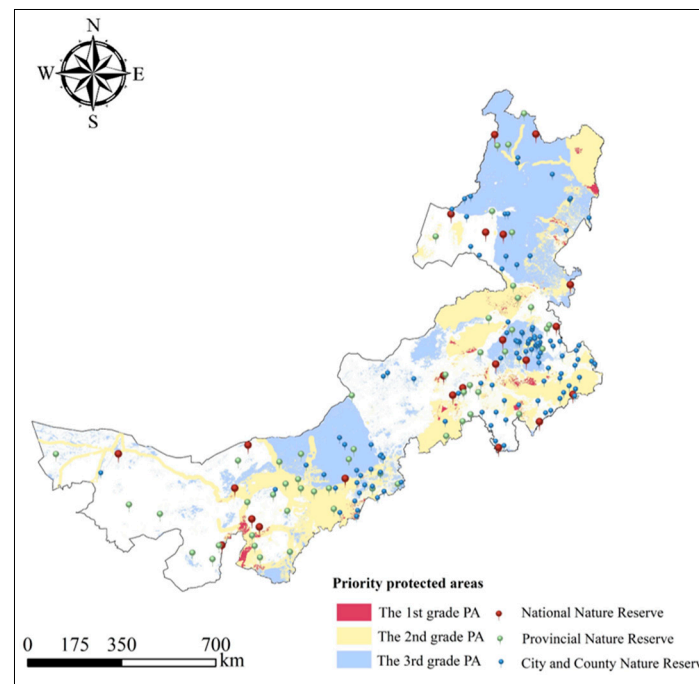


**Figure 11.** Distribution of Nature Reserves in Inner Mongolia.

**Table 4.** Primary hotspot protection areas.

First-Class Protection Priority Area Name (A1–A12)	District	Regional Details
A1 Dobao Shan Town Nature Reserve	Heihe City, Dobao Shan Town	There are 1880 km <sup>2</sup> of woodland in Dobao Shan town, with 19,457,600 cubic meters of standing wood, mainly larch, poplar, linden, Quercus, and birch. The vegetation cover is high and the biodiversity is outstanding, most of the area is in a natural wild state.
A2 Molidawa Bayan Wetland Ecosystem Reserve	Hulunbuir City, Molidawa Daur autonomous Banner, Bayan Ewen National Township	Molidawa Bayan National Wetland Park has a wetland area of 30,168 km <sup>2</sup> , bringing together a number of regional biota compositions such as the Daxinganling, Mongolian Plateau, Songliao Plain, Changbai Mountain, and North China in China, and has outstanding biodiversity.

Table 4. Cont.

First-Class Protection Priority Area Name (A1–A12)	District	Regional Details
A3 (a) Wildlife Nature Reserve in southeastern Chabach Township	(a) Hulunbuir City, Arrong Banner, Chabach Ewenke National Township	The area under the jurisdiction of Chabach Township is 164 km <sup>2</sup> of arable land, 370 km <sup>2</sup> of forest land, and 186.67 km <sup>2</sup> of pasture. Rich forestry resources, large areas of forests provide living conditions for wild animals, mainly moose, horse deer, brown bear, roe deer, wild boar, lynx, snow rabbits, pheasants, flying dragons, and other wild animals. Wolniuhe Town has 1.054 km <sup>2</sup> of forest, 75.27% forest coverage, and 186.67 km <sup>2</sup> of pasture. The territory has abundant water resources, fertile land and mild climate.
A3 (b) Forest Ecosystem and Wildlife Reserve in the South of Zalantun, Wolniuhe Township	(b) Hulunbuir City, Arong Banner, Woliuhe Town,	There are wild plants and herbs such as mushroom, fern, yellow flowering cabbage, monkey fungus, hazelnut, etc. There are also many kinds of wild animals protected by the state such as mountain rabbit, wild boar, roe deer, wild song, flying dragon, etc. Mengelhan Mountain Nature Reserve, a provincial-level nature reserve, is located at the South of the Daxinganling Mountains and in the northern part of Horqin Grassland. Its total area is 212.17 km <sup>2</sup> . The main objects of protection are natural secondary forests, grassland meadow ecosystems, and rare wildlife and plants.
A4 (a) Mengelhan Mountain Nature Reserve *	Hinggan League, Horqin Right Wing Banner, Ulanmadu Sumxiang	Ulan River Nature Reserve is a provincial-level nature reserve. The total area is 585.15 km <sup>2</sup> and the main protection object is the water-conserving forest.
A4 (b) Ulan River Nature Reserve *	Hinggan League, Horqin Right Wing Banner.	With a total area of more than 70,000 km <sup>2</sup> , the Urumqi grassland has been designated as a “National Key Ecological Function Area”.
A5 Bayanhusumxiang Central Grassland Ecosystem Reserve	Xilin Gol league, West Ujimqin Banner, Bayanhu shumxiang.	Baoligansumu is part of the Inner Mongolia Plateau and has a complete grassland type, namely meadow grassland, typical grassland, semi-desert grassland, and sandy grassland, with more than 1200 kinds of plants on the ground.
A6 Baoligeng Northeast Grassland Ecosystem Reserve	Chifeng City, Xilinhot City Baoligansumu.	The northern part of Balachi Zhongde is dominated by the reforestation of barren hills and the southern part is dominated by the great reforestation of Wanli, with a construction area of more than 200 km <sup>2</sup> .
A7 (a) South-central Balach Ruud Sumu Grassland Ecosystem Reserve	Chifeng City, Aruqorchin Banner, Barachilde South Central	With a total area of 180 km <sup>2</sup> , the Xiaoheyuan Autonomous Region Wetland Bird Nature Reserve is a comprehensive nature reserve that focuses on protecting birds and the wetland ecosystem on which they depend.
A7 (b) Xiaoheyuan Autonomous Region-level Wetland Bird District Nature Reserve *	Chifeng City, Aohan Banner, Linxi Town,	

Table 4. Cont.

First-Class Protection Priority Area Name (A1–A12)	District	Regional Details
A8 Saiyinghuduga Sumu Northwest Grassland Ecosystem and Wildlife Reserve	Xilin Gol league Zhenglan banner, SaiyinHuduga Sumu	Saiyinghuduga Sumu is rich in wildlife resources, with 708 kinds of plants and more than 20 kinds of rare wildlife resources. The town has a forest area of 190 km <sup>2</sup> , with a forest coverage rate of 37%. The tree species are poplar, almond, elm, camphor pine, fruit trees, etc.
A9 (a) Forest Ecosystem Reserve in Uduntau Hai Town	Chifeng City, Wunniut Banner, Wuduntau Hai Town	The reserve covers an area of about 8 km <sup>2</sup> and is a protected area for wetland ecosystems and rare birds.
A9 (b) Wupaizi Nature Reserve *	Chifeng City, Wunniut Banner, Wupaizi Village	The reserve covers a total area of 3 km <sup>2</sup> and the main objects of protection are mountain forests, scrub ecosystems, and wild plants and animals.
A10 (a) Black Tiger Mountain-Eagle Beak Mountain Wildlife Nature Reserve *	Hohhot City, Qingshuihe County, Beibao Township	With a total area of 51.7 km <sup>2</sup> , the reserve is a comprehensive nature reserve with a variety of ecosystems such as mountain forests and thickets; rare wildlife and plants are the main objects of protection.
A10 (b) Qingshuihe County Shake Forest Gorge Nature Reserve *	Hohhot City, Qingshuihe County, Leekzhuang Township	Baiji Shaba Nature Reserve is a nationally known example of successful sand control and reforestation. The type of protection belongs to desert ecosystem and wildlife reserve.
A10 (c) Baiji Shaba Nature Reserve *	Hohhot City, Linge County	The total area of the reserve is 1448 km <sup>2</sup> . It is a nature reserve for wild plant types and protects endangered wild plant populations represented by Ural licorice and fragile desert steppe ecosystems and their biodiversity.
A11 Ortok Banner Licorice Nature Reserve *	Erdos City, Ortoge Banner	Shanghai Miao town is in the southwest of Ertok former banner, planting valuable the medicinal herbs including licorice (453.33 km <sup>2</sup> ) with high quality; wild medicinal herbs also include wintergreen, bitter ginseng, white tribulus terrestris, free silk, motherwort, and so on. The town can use 3280 km <sup>2</sup> of pasture, of which 1000 km <sup>2</sup> is for the rare plant species Tibetan broccoli.
A12 (a) Shanghai Miao Town Western Licorice Nature Reserve	Erdos City, Ortok Qianqi Banner, Shanghai Miao Town	This is a typical combination of agricultural and pastoral lands. The natural resources in the area mainly include Tibetan broccoli, licorice outside Liang, ephedra, gypsum, natural gas, oil, etc.
A12 (b) Olezaki Town Central Dashatou Desert Nature Reserve	Erdos City, Ortok Qianqi Banner, Olezhaoqi Town	

Specific Analysis of Primary Hotspot Protection Areas (\*: Existing Protection Areas).

## 5. Discussion

### 5.1. Comparative Analysis of Biodiversity Conservation Hotspot Areas

Biodiversity hotspots are areas with the greatest diversity of native species or high concentrations of endemic species [49], whereas the establishment of nature reserves is a priority for achieving the maximum conservation of regional biodiversity. In 1998, Myers identified 10 critical forest conservation areas based on the degree of endemism and threats to species such as vascular plants and terrestrial vertebrates and identified



25 global biodiversity hotspots, with 1.4% of the land area containing 44% of vascular plants and 35% of vertebrates. These areas are the richest in terms of species and cover 3.4% of the global land area and more than 60% of terrestrial species [50]. In 2010, the “China Biodiversity Conservation Strategy and Action Plan (2011–2030)”, which considers factors related to the conservation of ecosystems and species, designated 35 biodiversity conservation priority areas, including 32 terrestrial biodiversity conservation priority areas and 3 marine biodiversity conservation priority areas [51]. This is the most comprehensive and systematic priority area in the field of biodiversity conservation in China and has certain guiding significance for the national priority of biodiversity conservation. Five priority conservation areas were located in the study area: Daxinganling District, Xiaoxinganling District, Hulunbuir District, Western Ordos–Heranshan–Yinshan District, and Xilinguole Grassland District. However, the current priority conservation areas are still too large and lack operability for optimization of the conservation area network in Inner Mongolia.

According to data on nature reserves in China published in ArcGIS Online, there are 191 nature reserves in the Inner Mongolia Autonomous Region, including 23 national nature reserves, 52 provincial nature reserves, and 116 municipal and county nature reserves (Figure 11). Nature reserves are areas set aside by the state for special protection and management, including representative natural ecosystems, natural concentrated distribution areas of rare and endangered wildlife species, natural relics of special significance, and other protected objects on land, water, or sea. It is an ecosystem that comprises both biotic and abiotic environments. Based on the results of the biodiversity conservation hotspot areas identified in this study and overlaying them with the data of the nature reserves in the Inner Mongolia Autonomous Region, we found that most nature reserves are located in priority areas for biodiversity conservation; however, conservation gaps still persist.

By comparing with the primary hotspot protection areas (Table 4), it was found that the primary hotspot protection areas were not covered and that there were vacancies in the following areas: A2, A3 (a), A3 (b), A5, A6, A7, A8, A9, A12 (a), and A12 (b). These areas have a high concentration of conservation vacancies and corresponding actions should be taken to increase conservation efforts and reduce biodiversity loss. In the past, the delineation of protected areas was usually carried out by national, provincial, and municipal agencies through field surveys based on rare and endangered species or representative ecosystems. However, the hotspot areas identified in this study through the use of remote sensing monitoring technology have the characteristics of macroscopicity, rapidity, and repeatability and therefore have the advantages of shortening the time, expanding the scope of identification, and reducing the manpower input of the identification process. The results of the identification can be used to carry out comprehensive surveys and long-term dynamic monitoring of biodiversity in hotspot areas and to optimize vacancies in the existing protected areas. This approach, based on remote sensing technology, provides new ideas and methods for protected area planning and can support ecological conservation more efficiently.

## 5.2. Methods for Identifying Hotspot Areas for Biodiversity Conservation

The identification of biodiversity conservation hotspots is a common method for in situ conservation of biodiversity, and the results can provide a basis for decision making under limited conditions. As a method of identifying nature conservation sites, different types of hotspots also vary greatly, and hotspots of species richness, endemism, and endangerment show different geographical distributions [52–55]. Considering the differences in hotspot areas among different species groups, nature reserves are often located in more remote areas, whereas areas with more intensive human activities are often under protected; therefore, some scholars propose constructing irreplaceability and vulnerability priority indicators through systematic conservation planning methods [56]. The principle of the complementarity of biodiversity is considered to optimize the selection of biodiversity conservation areas while minimizing conservation costs and thus using limited resources to achieve clear conservation objectives [57,58]. In recent years, many foreign scholars have

used species distribution models to identify hotspots of protected species and formulate scientific and reasonable conservation plans. Using the MaxEnt model to identify the potential distribution of a single species and superimposing the potential distribution of multiple species, the richness of the species distribution within the study area can be obtained and conservation hotspots can be identified [59–61]. In addition, under the Ecological Red Line Conservation Initiative, it is recommended that future expansion of protected areas should take into account the threats of climate change and anthropogenic pressures to appropriately measure the priority of protected areas for conservation; scholars have already explored the impacts of climate change and human activities on biodiversity and conducted the delineation of conservation hotspot areas by quantifying climate change and human activities [37,39]. However, these studies only identified hotspot areas by focusing on a single dimension of climate change or human activities. In contrast, in this study, we produced biodiversity hotspot distribution maps for the spatial–temporal remote sensing index and the human footprint index and, by observing the results, we can find that the selection of the indices is based on different bases, which leads to differences in their spatial distributions. Therefore, we comprehensively considered the spatial–temporal remote sensing index and human footprint index and determined the final conservation hotspot areas based on the principle of spatial consistency through the superposition analysis of the indices. The hotspot area identification system constructed combines two influencing factors, considers both spatial and temporal scales, and improves the operability of the optimization of the regional protected area network, which is of some practical significance.

#### 5.2.1. Spatial–Temporal Remote Sensing Index and Biodiversity

High interannual variability in phenology and seasons poses a threat to the survival of many species; however, high spatial variability can enhance the survival of species under such threats. In this study, interannual and spatial variability indices were generated to characterize the interannual and seasonal variability and to identify high and low conservation hotspots for biodiversity conservation. This study found that there are significant differences in interannual and spatial variability among ecological regions and cities in Inner Mongolia, which shows that the risks posed by seasonal fluctuations in phenology and temperature vary depending on location. Hotspots of conservation related to climate and seasonal fluctuations were identified using a map of interannual and spatial variability, that is areas with high interannual variability posing high threats and areas with low spatial variability and low ecological resilience.

The interannual variability of the vegetation index EVI and the surface temperature LST in the Inner Mongolia Autonomous Region were found to be quite different based on the results of the spatial–temporal remote sensing indices. The correlation between the interannual variability of EVI  $T\_CV\_E_s$  and the interannual variability of LST  $T\_CV\_L_s$  was weak for the entire Inner Mongolian province and in most ecological zones. However, moderate positive and negative correlations were observed in some ecoregions and small areas. Some of the explanations for the weak and moderate associations may be that vegetation growth has adapted to the rapid temperature rise and is less affected by climate change because Inner Mongolia's ecoregions are diverse in terms of flora and topography [62] or because of geographic influences. The delayed reaction of vegetation to precipitation may also be a factor [63], and this relationship is influenced by the vegetation type [64,65].

MODIS EVI and LST long timeseries data were used to calculate interannual variability in phenology and seasonal indicators. The timeseries of vegetation indices are derived from the majority of phenological indicators [66]; however, in areas with little vegetation, vegetation indices are occasionally unable to identify phenological variation patterns. In areas with similarities in vegetation phenology and temperature seasonality, changes in the LST can play a complementary role, for example, in areas such as evergreen forests, where changes in the LST provide better estimates of seasonal SOS and EOS due to limited changes in greenness [67]. Temperature changes or temperature seasonality may result from

climate change, although documenting seasonal fluctuations alone does not adequately capture the whole impact of this phenomenon; the 20-year MODIS data records climate change over a fairly short period of time, so this study did not conduct a trend analysis and chose to focus on seasonal changes, which may lead to higher climate change and more frequent extreme events. Despite its limitations, satellite remote sensing is the only data source capable of mapping vegetation phenology over large areas and that can be used to quantify the threats posed to biodiversity by climate change.

#### 5.2.2. Human Footprint Index and Biodiversity

Compared with natural factors, such as climate, anthropogenic factors can also have a positive or negative effect on changes in biodiversity in nature reserves, which, in turn, affects the effectiveness of biodiversity conservation. Although the establishment of nature reserves has mitigated the effects of anthropogenic disturbances to some extent [68,69], an increase in anthropogenic disturbances has a clear impact on nature reserves in terms of the conservation of ecosystems [69] and species [70]. The combination of anthropogenic disturbances and climate change has been the most important factor in the conservation of Natural World Heritage Sites.

In this study, only population density, grazing density, land use data, nighttime lights, and traffic accessibility factors were considered in the calculation of the human footprint index; other factors affecting human activities and socioeconomic construction (such as the duration of disturbing activities and disturbances from human activities, such as pollution and invasive alien species) were not accounted for [37,71,72]. Therefore, the index system must be further improved. Additionally, the lack of available data can lead to certain anthropogenic pressures remaining constant over time. If these pressures expand at a higher-than-average rate, it will lead to an underestimation of the expansion of the human footprint. Lastly, the human footprint measures the pressure of human activities on nature rather than the realized state or impact on natural systems or their biodiversity. The main objective of this study was to update the human footprint map to provide a contemporary view of human pressures so that the spatial patterns of human activities in Inner Mongolia can be analyzed and the intensity of human activities can be quantified for the most recent years.

## 6. Conclusions

The results of this study show that climate change and the human footprint significantly affect biodiversity levels in Inner Mongolia. Firstly, spatial-temporal remote sensing indices were generated by calculating the interannual and spatial variability of the EVI and LST in Inner Mongolia over the 20-year period 2002–2021 to identify biodiversity conservation hotspots induced by rapid climate change, i.e., areas with high threat due to high interannual variability and high spatial variability with high resilience. Secondly, a human footprint map of Inner Mongolia in 2021 was generated to determine the intensity of human activities in the region and the hotspot protected areas, i.e., areas with high human activities, which are mostly located in urban construction areas, arable land, and road construction areas. Finally, biodiversity is more likely to be threatened in areas with greater degrees of climate change and higher anthropogenic pressures than in areas with milder climate change and lower anthropogenic pressures, so we combined the two indices mentioned above to analyze the hotspot areas in a stacked combination and delineated three levels of priority protected areas.

In the framework of this study, we identify biodiversity conservation hotspots in two dimensions: climate change and human activities. We provide a large-scale, more balanced, and comprehensive approach to identifying hotspots than previous identifications based on a single dimension or on data from certain species. Remote sensing allows us to identify biodiversity conservation hotspots at large scales in other regions and also includes hotspots for climate change and human activities. In addition, the framework helps to identify the best areas for the future expansion of protected areas and prioritize their

expansion. It can help us take timely and proactive measures to maintain biodiversity and ecosystem integrity.

**Author Contributions:** Conceptualization, Y.L. and H.W.; funding acquisition, H.W.; methodology, Y.L.; supervision, H.W.; Data curation, Y.L.; validation, Y.L.; visualization, H.T., J.L., and J.S.; Writing—original draft, Y.L.; Writing—review and edit, Y.L., H.W., Y.Z., X.Z., T.Q., D.L., and Y.Y. All authors have read and agreed to the published version of the manuscript.

**Funding:** This research was funded by the Key Science and Technology Project of Inner Mongolia (2021ZD0011-5).

**Institutional Review Board Statement:** Not applicable.

**Data Availability Statement:** Not applicable.

**Conflicts of Interest:** The authors declare no conflict of interest.

## References

1. Butchart, S.H.M.; Walpole, M.; Collen, B.; van Strien, A.; Scharlemann, J.P.W.; Almond, R.E.A.; Baillie, J.E.M.; Bomhard, B.; Brown, C.; Bruno, J.; et al. Global Biodiversity: Indicators of Recent Declines. *Science* **2010**, *328*, 1164–1168. [\[CrossRef\]](#)
2. Lewis, E.; MacSharry, B.; Juffe-Bignoli, D.; Harris, N.; Burrows, G.; Kingston, N.; Burgess, N.D. Dynamics in the global protected-area estate since 2004. *Conserv. Biol.* **2019**, *33*, 570–579. [\[CrossRef\]](#) [\[PubMed\]](#)
3. Gray, C.L.; Hill, S.L.L.; Newbold, T.; Hudson, L.N.; Borger, L.; Contu, S.; Hoskins, A.J.; Ferrier, S.; Purvis, A.; Scharlemann, J.P.W. Local biodiversity is higher inside than outside terrestrial protected areas worldwide. *Nat. Commun.* **2016**, *7*, 12306. [\[CrossRef\]](#) [\[PubMed\]](#)
4. Larsen, F.W.; Turner, W.R.; Mittermeier, R.A. Will protection of 17% of land by 2020 be enough to safeguard biodiversity and critical ecosystem services? *Oryx* **2015**, *49*, 74–79. [\[CrossRef\]](#)
5. Pimm, S.L.; Jenkins, C.N.; Li, B.V. How to protect half of Earth to ensure it protects sufficient biodiversity. *Sci. Adv.* **2018**, *4*, eaat2616. [\[CrossRef\]](#) [\[PubMed\]](#)
6. Jetz, W.; McGeoch, M.A.; Guralnick, R.; Ferrier, S.; Beck, J.; Costello, M.; Fernandez, M.; Geller, G.N.; Keil, P.; Merow, C.; et al. Essential biodiversity variables for mapping and monitoring species populations. *Nat. Ecol. Evol.* **2019**, *3*, 539–551. [\[CrossRef\]](#) [\[PubMed\]](#)
7. Pereira, H.M.; Leadley, P.W.; Proenca, V.; Alkemade, R.; Scharlemann, J.P.W.; Fernandez-Manjarres, J.F.; Araujo, M.B.; Balvanera, P.; Biggs, R.; Cheung, W.W.L.; et al. Scenarios for Global Biodiversity in the 21st Century. *Science* **2010**, *330*, 1496–1501. [\[CrossRef\]](#)
8. Read, Q.D.; Zarnetske, P.L.; Record, S.; Dahlin, K.M.; Costanza, J.K.; Finley, A.O.; Gaddis, K.D.; Grady, J.M.; Hobi, M.L.; Latimer, A.M.; et al. Beyond counts and averages: Relating geodiversity to dimensions of biodiversity. *Glob. Ecol. Biogeogr.* **2020**, *29*, 696–710. [\[CrossRef\]](#)
9. Zarnetske, P.L.; Read, Q.D.; Record, S.; Gaddis, K.D.; Pau, S.; Hobi, M.L.; Malone, S.L.; Costanza, J.; Dahlin, K.M.; Latimer, A.M.; et al. Towards connecting biodiversity and geodiversity across scales with satellite remote sensing. *Glob. Ecol. Biogeogr.* **2019**, *28*, 548–556. [\[CrossRef\]](#)
10. Wan, X.; Jiang, G.; Yan, C.; He, F.; Wen, R.; Gu, J.; Li, X.; Ma, J.; Stenseth, N.C.; Zhang, Z. Historical records reveal the distinctive associations of human disturbance and extreme climate change with local extinction of mammals. *Proc. Natl. Acad. Sci. USA* **2019**, *116*, 19001–19008. [\[CrossRef\]](#)
11. Thuiller, W.; Lavorel, S.; Araujo, M.B.; Sykes, M.T.; Prentice, I.C. Climate change threats to plant diversity in Europe. *Proc. Natl. Acad. Sci. USA* **2005**, *102*, 8245–8250. [\[CrossRef\]](#) [\[PubMed\]](#)
12. Zhang, Y.; Loreau, M.; He, N.; Wang, J.; Pan, Q.; Bai, Y.; Han, X. Climate variability decreases species richness and community stability in a temperate grassland. *Oecologia* **2018**, *188*, 183–192. [\[CrossRef\]](#) [\[PubMed\]](#)
13. Bongaarts, J. Summary for policymakers of the global assessment report on biodiversity and ecosystem services of the Intergovernmental Science-Policy Platform on Biodiversity and Ecosystem Services. *Popul. Dev. Rev.* **2019**, *45*, 680–681. [\[CrossRef\]](#)
14. Ma, X.; Huete, A.; Yu, Q.; Coupe, N.R.; Davies, K.; Broich, M.; Ratana, P.; Beringer, J.; Hutley, L.B.; Cleverly, J.; et al. Spatial patterns and temporal dynamics in savanna vegetation phenology across the North Australian Tropical Transect. *Remote Sens. Environ.* **2013**, *139*, 97–115. [\[CrossRef\]](#)
15. Mann, M.E.; Park, J. Greenhouse warming and changes in the seasonal cycle of temperature: Model versus observations. *Geophys. Res. Lett.* **1996**, *23*, 1111–1114. [\[CrossRef\]](#)
16. Renner, S.S.; Zohner, C.M. Climate Change and Phenological Mismatch in Trophic Interactions Among Plants, Insects, and Vertebrates. *Annu. Rev. Ecol. Evol. Syst.* **2018**, *49*, 165–182. [\[CrossRef\]](#)
17. Glennon, M.J.; Langdon, S.F.; Rubenstein, M.A.; Cross, M.S. Temporal changes in avian community composition in lowland conifer habitats at the southern edge of the boreal zone in the Adirondack Park, NY. *PLoS ONE* **2019**, *14*, e0220927. [\[CrossRef\]](#) [\[PubMed\]](#)
18. Socolar, J.B.; Epanchin, P.N.; Beissinger, S.R.; Tingley, M.W. Phenological shifts conserve thermal niches in North American birds and reshape expectations for climate-driven range shifts. *Proc. Natl. Acad. Sci. USA* **2017**, *114*, 12976–12981. [\[CrossRef\]](#) [\[PubMed\]](#)



19. Pearce-Higgins, J.W.; Eglington, S.M.; Martay, B.; Chamberlain, D.E. Drivers of climate change impacts on bird communities. *J. Ecol.* **2015**, *84*, 943–954. [[CrossRef](#)]
20. Nystrom, M.; Folke, C. Spatial resilience of coral reefs. *Ecosystems* **2001**, *4*, 406–417. [[CrossRef](#)]
21. Oliver, T.H.; Heard, M.S.; Isaac, N.J.B.; Roy, D.B.; Procter, D.; Eigenbrod, F.; Freckleton, R.; Hector, A.; Orme, C.D.L.; Petchey, O.L.; et al. Biodiversity and Resilience of Ecosystem Functions. *Trends Ecol. Evol.* **2015**, *30*, 673–684. [[CrossRef](#)]
22. Gunderson, L.; Folke, C. Resilience—Now more than ever. *Ecol. Soc.* **2005**, *10*, 22. [[CrossRef](#)]
23. Virah-Sawmy, M.; Gillson, L.; Willis, K.J. How does spatial heterogeneity influence resilience to climatic changes? Ecological dynamics in southeast Madagascar. *Ecol. Monogr.* **2009**, *79*, 557–574. [[CrossRef](#)]
24. Keppel, G.; Van Niel, K.P.; Wardell-Johnson, G.W.; Yates, C.J.; Byrne, M.; Mucina, L.; Schut, A.G.T.; Hopper, S.D.; Franklin, S.E. Refugia: Identifying and understanding safe havens for biodiversity under climate change. *Glob. Ecol. Biogeogr.* **2012**, *21*, 393–404. [[CrossRef](#)]
25. Elsen, P.R.; Farwell, L.S.; Pidgeon, A.M.; Radeloff, V.C. Contrasting seasonal patterns of relative temperature and thermal heterogeneity and their influence on breeding and winter bird richness patterns across the conterminous United States. *Ecography* **2021**, *44*, 953–965. [[CrossRef](#)]
26. Hmimina, G.; Dufrene, E.; Pontailier, J.Y.; Delpierre, N.; Aubinet, M.; Caquet, B.; de Grandcourt, A.; Burban, B.; Flechard, C.; Granier, A.; et al. Evaluation of the potential of MODIS satellite data to predict vegetation phenology in different biomes: An investigation using ground-based NDVI measurements. *Remote Sens. Environ.* **2013**, *132*, 145–158. [[CrossRef](#)]
27. Hengl, T.; Heuvelink, G.B.M.; Tadic, M.P.; Pebesma, E.J. Spatio-temporal prediction of daily temperatures using time-series of MODIS LST images. *Theor. Appl. Climatol.* **2012**, *107*, 265–277. [[CrossRef](#)]
28. Hu, Q.; Sulla-Menashe, D.; Xu, B.; Yin, H.; Tang, H.; Yang, P.; Wu, W. A phenology-based spectral and temporal feature selection method for crop mapping from satellite time series. *Int. J. Appl. Earth Obs. Geoinf.* **2019**, *80*, 218–229. [[CrossRef](#)]
29. Farwell, L.S.; Elsen, P.R.; Razenkova, E.; Pidgeon, A.M.; Radeloff, V.C. Habitat heterogeneity captured by 30-m resolution satellite image texture predicts bird richness across the United States. *Ecol. Appl.* **2020**, *30*, e02157. [[CrossRef](#)]
30. Wood, E.M.; Pidgeon, A.M.; Radeloff, V.C.; Keuler, N.S. Image Texture Predicts Avian Density and Species Richness. *PLoS ONE* **2013**, *8*, e63211. [[CrossRef](#)]
31. Elsen, P.R.; Farwell, L.S.; Pidgeon, A.M.; Radeloff, V.C. Landsat 8 TIRS-derived relative temperature and thermal heterogeneity predict winter bird species richness patterns across the conterminous United States. *Remote Sens. Environ.* **2020**, *236*, 111514. [[CrossRef](#)]
32. Strassburg, B.B.N.; Iribarrem, A.; Beyer, H.L.; Cordeiro, C.L.; Crouzeilles, R.; Jakovac, C.C.; Braga Junqueira, A.; Lacerda, E.; Latawiec, A.E.; Balmford, A.; et al. Global priority areas for ecosystem restoration. *Nature* **2020**, *586*, 724–729. [[CrossRef](#)]
33. Shrestha, N.; Xu, X.; Meng, J.; Wang, Z. Vulnerabilities of protected lands in the face of climate and human footprint changes. *Nat. Commun.* **2021**, *12*, 1632. [[CrossRef](#)] [[PubMed](#)]
34. Kennedy, C.M.; Oakleaf, J.R.; Theobald, D.M.; Baruch-Mordo, S.; Kiesecker, J. Managing the middle: A shift in conservation priorities based on the global human modification gradient. *Glob. Change Biol.* **2019**, *25*, 811–826. [[CrossRef](#)] [[PubMed](#)]
35. Wang, K.; Wang, C.; Feng, X.; Wu, X.; Fu, B. Research progress on the relationship between biodiversity and ecosystem multifunctionality. *Acta Ecol. Sin.* **2022**, *42*, 11–23.
36. Young, H.S.; McCauley, D.J.; Galetti, M.; Dirzo, R. Patterns, Causes, and Consequences of Anthropocene Defaunation. *Annu. Rev. Ecol. Syst.* **2016**, *47*, 333–358. [[CrossRef](#)]
37. Venter, O.; Sanderson, E.W.; Magrath, A.; Allan, J.R.; Beher, J.; Jones, K.R.; Possingham, H.P.; Laurance, W.F.; Wood, P.; Fekete, B.M.; et al. Sixteen years of change in the global terrestrial human footprint and implications for biodiversity conservation. *Nat. Commun.* **2016**, *7*, 12558. [[CrossRef](#)] [[PubMed](#)]
38. Wei, Q.; Abudurehman, M.; Halike, A.; Yao, K.; Yao, L.; Tang, H.; Tuheiti, B. Temporal and spatial variation analysis of habitat quality on the PLUS-InVEST model for Ebinur Lake Basin, China. *Ecol. Indic.* **2022**, *145*, 109632. [[CrossRef](#)]
39. Silveira, E.M.O.; Radeloff, V.C.; Martinuzzi, S.; Martinez Pastur, G.J.; Rivera, L.O.; Politi, N.; Lizarraga, L.; Farwell, L.S.; Elsen, P.R.; Pidgeon, A.M. Spatio-temporal remotely sensed indices identify hotspots of biodiversity conservation concern. *Remote Sens. Environ.* **2021**, *258*, 112368. [[CrossRef](#)]
40. Correa Ayram, C.A.; Etter, A.; Diaz-Timote, J.; Rodriguez Buritica, S.; Ramirez, W.; Corzo, G. Spatiotemporal evaluation of the human footprint in Colombia: Four decades of anthropic impact in highly biodiverse ecosystems. *Ecol. Indic.* **2020**, *117*, 106630. [[CrossRef](#)]
41. Getis, A.; Ord, J.K. The analysis of spatial association by use of distance statistics. *Geogr. Anal.* **1992**, *24*, 189–206. [[CrossRef](#)]
42. Clarke, A.; Gaston, K.J. Climate, energy and diversity. *Proc. R. Soc. B-Biol. Sci.* **2006**, *273*, 2257–2266. [[CrossRef](#)]
43. Wei, Q.; Halike, A.; Yao, K.; Chen, L.; Balati, M. Construction and optimization of ecological security pattern in Ebinur Lake Basin based on MSPA-MCR models. *Ecol. Indic.* **2022**, *138*, 108857. [[CrossRef](#)]
44. Xiao, W.; Lv, X.; Zhao, Y.; Sun, H.; Li, J. Ecological resilience assessment of an arid coal mining area using index of entropy and linear weighted analysis: A case study of Shendong Coalfield, China. *Ecol. Indic.* **2020**, *109*, 105843. [[CrossRef](#)]
45. Duan, Q.; Luo, L. A dataset of human footprint over the Qinghai-Tibet Plateau during 1990–2015. *China Sci. Data* **2020**, *5*, 303–312.
46. Wu, Y.; Shi, K.; Chen, Z.; Liu, S.; Chang, Z. Developing Improved Time-Series DMSP-OLS-Like Data (19922019) in China by Integrating DMSP-OLS and SNPP-VIIRS. *IEEE Trans. Geosci. Remote Sens.* **2022**, *60*, 1–14. [[CrossRef](#)]



47. Huang, X.; Wu, Z.; Zhang, Q.; Cao, Z.; Zheng, Z.; He, J. Wetland resources distribution and important wetland recognition of Guangdong-Hong Kong-Macao Greater Bay Area based on human pressure index. *J. Nat. Resour.* **2022**, *37*, 1961–1974. [\[CrossRef\]](#)
48. Xu, Y.; Sun, X.; Tang, Q. Human activity intensity of land surface: Concept, method and application in China. *Acta Geogr. Sin.* **2015**, *70*, 1068–1079. [\[CrossRef\]](#)
49. Myers, N. Threatened biotas: “hot spots” in tropical forests. *Environmentalist* **1988**, *8*, 187–208. [\[CrossRef\]](#) [\[PubMed\]](#)
50. Myers, N.; Mittermeier, R.A.; Mittermeier, C.G.; da Fonseca, G.A.B.; Kent, J. Biodiversity hotspots for conservation priorities. *Nature* **2000**, *403*, 853–858. [\[CrossRef\]](#)
51. Dayuan, X. The main content and implementation strategy for China Biodiversity Conservation Strategy and Action Plan. *Biodivers. Sci.* **2011**, *19*, 387–388. [\[CrossRef\]](#)
52. Lamoreux, J.F.; Morrison, J.C.; Ricketts, T.H.; Olson, D.M.; Dinerstein, E.; McKnight, M.W.; Shugart, H.H. Global tests of biodiversity concordance and the importance of endemism. *Nature* **2006**, *440*, 212–214. [\[CrossRef\]](#)
53. Pollock, L.J.; Thuiller, W.; Jetz, W. Large conservation gains possible for global biodiversity facets. *Nature* **2017**, *546*, 141–144. [\[CrossRef\]](#) [\[PubMed\]](#)
54. Orme, C.D.L.; Davies, R.G.; Burgess, M.; Eigenbrod, F.; Pickup, N.; Olson, V.A.; Webster, A.J.; Ding, T.S.; Rasmussen, P.C.; Ridgely, R.S.; et al. Global hotspots of species richness are not congruent with endemism or threat. *Nature* **2005**, *436*, 1016–1019. [\[CrossRef\]](#) [\[PubMed\]](#)
55. Grenyer, R.; Orme, C.D.L.; Jackson, S.F.; Thomas, G.H.; Davies, R.G.; Davies, T.J.; Jones, K.E.; Olson, V.A.; Ridgely, R.S.; Rasmussen, P.C.; et al. Global distribution and conservation of rare and threatened vertebrates. *Nature* **2006**, *444*, 93–96. [\[CrossRef\]](#) [\[PubMed\]](#)
56. Brooks, T.M.; Mittermeier, R.A.; da Fonseca, G.A.B.; Gerlach, J.; Hoffmann, M.; Lamoreux, J.F.; Mittermeier, C.G.; Pilgrim, J.D.; Rodrigues, A.S.L. Global biodiversity conservation priorities. *Science* **2006**, *313*, 58–61. [\[CrossRef\]](#) [\[PubMed\]](#)
57. Margules, C.R.; Pressey, R.L. Systematic conservation planning. *Nature* **2000**, *405*, 243–253. [\[CrossRef\]](#) [\[PubMed\]](#)
58. McIntosh, E.J.; Pressey, R.L.; Lloyd, S.; Smith, R.J.; Grenyer, R. The Impact of Systematic Conservation Planning. *Annu. Rev. Ecol. Evol. Syst.* **2017**, *42*, 677–697.
59. Fourcade, Y.; Engler, J.O.; Roedder, D.; Secondi, J. Mapping Species Distributions with MAXENT Using a Geographically Biased Sample of Presence Data: A Performance Assessment of Methods for Correcting Sampling Bias. *PLoS ONE* **2014**, *9*, e97122. [\[CrossRef\]](#) [\[PubMed\]](#)
60. Jones, M.C.; Cheung, W.W.L. Multi-model ensemble projections of climate change effects on global marine biodiversity. *ICES J. Mar. Sci.* **2015**, *72*, 741–752. [\[CrossRef\]](#)
61. Melo-Merino, S.M.; Reyes-Bonilla, H.; Lira-Noriega, A. Ecological niche models and species distribution models in marine environments: A literature review and spatial analysis of evidence. *Ecol. Model.* **2020**, *415*, 108837. [\[CrossRef\]](#)
62. Hikosaka, K.; Ishikawa, K.; Borjigidai, A.; Muller, O.; Onoda, Y. Temperature acclimation of photosynthesis: Mechanisms involved in the changes in temperature dependence of photosynthetic rate. *J. Exp. Bot.* **2006**, *57*, 291–302. [\[CrossRef\]](#)
63. An, S.; Zhu, X.; Shen, M.; Wang, Y.; Cao, R.; Chen, X.; Yang, W.; Chen, J.; Tang, Y. Mismatch in elevational shifts between satellite observed vegetation greenness and temperature isolines during 2000–2016 on the Tibetan Plateau. *Glob. Change Biol.* **2018**, *24*, 5411–5425. [\[CrossRef\]](#)
64. Liu, H.; Zhang, M.; Lin, Z.; Xu, X. Spatial heterogeneity of the relationship between vegetation dynamics and climate change and their driving forces at multiple time scales in Southwest China. *Agric. For. Meteorol.* **2018**, *256*, 10–21. [\[CrossRef\]](#)
65. Wang, J.; Meng, J.J.; Cai, Y.L. Assessing vegetation dynamics impacted by climate change in the southwestern karst region of China with AVHRR NDVI and AVHRR NPP time-series. *Environ. Geol.* **2008**, *54*, 1185–1195. [\[CrossRef\]](#)
66. Zeng, L.; Wardlow, B.D.; Xiang, D.; Hu, S.; Li, D. A review of vegetation phenological metrics extraction using time-series, multispectral satellite data. *Remote Sens. Environ.* **2020**, *237*, 111511. [\[CrossRef\]](#)
67. Liu, Y.; Wu, C.; Peng, D.; Xu, S.; Gonsamo, A.; Jassal, R.S.; Arain, M.A.; Lu, L.; Fang, B.; Chen, J.M. Improved modeling of land surface phenology using MODIS land surface reflectance and temperature at evergreen needleleaf forests of central North America. *Remote Sens. Environ.* **2016**, *176*, 152–162. [\[CrossRef\]](#)
68. Guette, A.; Godet, L.; Juigner, M.; Robin, M. Worldwide increase in Artificial Light At Night around protected areas and within biodiversity hotspots. *Biol. Conserv.* **2018**, *223*, 97–103. [\[CrossRef\]](#)
69. Feng, C.-T.; Cao, M.; Liu, F.-Z.; Zhou, Y.; Du, J.-H.; Zhang, L.-B.; Huang, W.-J.; Luo, J.-W.; Li, J.-S.; Wang, W. Improving protected area effectiveness through consideration of different human-pressure baselines. *Conserv. Biol.* **2022**, *36*, e13887. [\[CrossRef\]](#) [\[PubMed\]](#)
70. Wei, W.; Swaisgood, R.R.; Pilfold, N.W.; Owen, M.A.; Dai, Q.; Wei, F.; Han, H.; Yang, Z.; Yang, X.; Gu, X.; et al. Assessing the Effectiveness of China’s Panda Protection System. *Curr. Biol.* **2020**, *30*, 1280.e2–1286.e2. [\[CrossRef\]](#) [\[PubMed\]](#)
71. Spear, D.; Foxcroft, L.C.; Bezuidenhout, H.; McGeoch, M.A. Human population density explains alien species richness in protected areas. *Biol. Conserv.* **2013**, *159*, 137–147. [\[CrossRef\]](#)
72. Venter, O.; Sanderson, E.W.; Magrath, A.; Allan, J.R.; Beher, J.; Jones, K.R.; Possingham, H.P.; Laurance, W.F.; Wood, P.; Fekete, B.M.; et al. Global terrestrial Human Footprint maps for 1993 and 2009. *Sci. Data* **2016**, *3*, 160067. [\[CrossRef\]](#)

**Disclaimer/Publisher’s Note:** The statements, opinions and data contained in all publications are solely those of the individual author(s) and contributor(s) and not of MDPI and/or the editor(s). MDPI and/or the editor(s) disclaim responsibility for any injury to people or property resulting from any ideas, methods, instructions or products referred to in the content.